JACS
JOURNAL OF THE AMERICAN CHEMICAL SOCIETY
Article
pubs.acs.org/JACS

Stepwise Protonation and Electron-Transfer Reduction of a Primary Copper−Dioxygen Adduct

Ryan L. Peterson,[†] Jake W. Ginsbach,[‡] Ryan E. Cowley,[‡] Munzarin F. Qayyum,[‡] Richard A. Himes,[†] Maxime A. Siegler,[†] Cathy D. Moore,[†] Britt Hedman,[§] Keith O. Hodgson,[‡,§] Shunichi Fukuzumi,[∥] Edward I. Solomon,*[,‡] and Kenneth D. Karlin*[,†]

[†]Johns Hopkins University, Baltimore, Maryland 21218, United States
[‡]Department of Chemistry, Stanford University, Stanford, California 94305, United States
[§]Stanford Synchrotron Radiation Lightsource, SLAC, Stanford University, Stanford, California 94305, United States
[∥]Department of Material and Life Science, Graduate School of Engineering, Osaka University, and ALCA, Japan Science and Technology Agency (JST), Suita, Osaka 565-0871, Japan

Supporting Information

ABSTRACT: The protonation−reduction of a dioxygen adduct with $[LCu^{I}][B(C_6F_5)_4]$, cupric superoxo complex $[LCu^{II}(O_2^{\bullet-})]^+$ (**1**) (L = TMG_3tren (1,1,1-tris[2-[N^2-(1,1,3,3-tetramethylguanidino)]ethyl]amine)) has been investigated. Trifluoroacetic acid ($HOAc_F$) reversibly associates with the superoxo ligand in ($[LCu^{II}(O_2^{\bullet-})]^+$) in a 1:1 adduct $[LCu^{II}(O_2^{\bullet-})(HOAc_F)]^+$ (**2**), as characterized by UV−visible, resonance Raman (rR), nuclear magnetic resonance (NMR), and X-ray absorption (XAS) spectroscopies, along with density functional theory (DFT) calculations. Chemical studies reveal that for the binding of $HOAc_F$ with **1** to give **2**, $K_{eq} = 1.2 \times 10^5$ M^{-1} (−130 °C) and $\Delta H^o = -6.9(7)$ kcal/mol, $\Delta S^o = -26(4)$ cal mol^{-1} K^{-1}). Vibrational (rR) data reveal a significant increase (29 cm^{-1}) in ν_{O-O} (= 1149 cm^{-1}) compared to that known for $[LCu^{II}(O_2^{\bullet-})]^+$ (**1**). Along with results obtained from XAS and DFT calculations, hydrogen bonding of $HOAc_F$ to a superoxo O-atom in **2** is established. Results from NMR spectroscopy of **2** at −120 °C in 2-methyltetrahydrofuran are also consistent with **1**/$HOAc_F$ = 1:1 formulation of **2** and with this complex possessing a triplet (S = 1) ground state electronic configuration, as previously determined for **1**. The pre-equilibrium acid association to **1** is followed by outer-sphere electron-transfer reduction of **2** by decamethylferrocene ($Me_{10}Fc$) or octamethylferrocene (Me_8Fc), leading to the products H_2O_2, the corresponding ferrocenium salt, and $[LCu^{II}(OAc_F)]^+$. Second-order rate constants for electron transfer (k_{et}) were determined to be 1365 M^{-1} s^{-1} ($Me_{10}Fc$) and 225 M^{-1} s^{-1} (Me_8Fc) at −80 °C. The (bio)chemical relevance of the proton-triggered reduction of the metal-bound dioxygen-derived fragment is discussed.

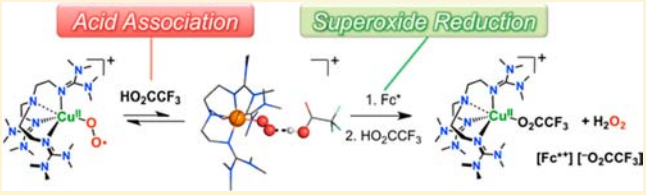

1. INTRODUCTION

The reduction and protonation of molecular oxygen (dioxygen, O_2) to hydrogen peroxide or water is a critical component of "dioxygen activation" chemistry effected by transition metal ions, i.e., for use of O_2 as an energy source in fuel cell applications ($O_2 + 4e^- + 4H^+ \rightarrow 2H_2O$)[1,2] or in oxidative chemistries including oxygen-atom transfer from O_2 to substrates (e.g., as in monooxygenases such as cytochrome P450;[3] R−H + O_2 + $2H^+$ + $2e^-$ → R−OH + H_2O), dehydrogenation ($SH_2 + O_2 \rightarrow S + H_2O_2$) or oxidase reactions (e.g., $4AH + O_2 \rightarrow 4A + 2H_2O$).[3a,4] As relevant to these processes, considerable insight can be obtained from copper metalloenzyme studies[5] which perform these biologically essential functions including the use of molecular oxygen for the functionalization/incorporation of oxygen atom(s) into organic substrates,[5a,b,6] the production of signaling agents,[5b,6b,7] or regulation of cellular energy flux through the utilization of dioxygen as a terminal electron acceptor.[8] Nature has evolved to include a diverse repertoire of copper active site configurations containing one to four copper ions with some possessing another redox active site to facilitate dioxygen reduction chemistries in oxidase and oxygenase systems.

For this variety of copper enzymes involved in O_2 processing, partly reduced dioxygen species (e.g., superoxo $O_2^{\bullet-}$ or peroxo O_2^{2-}) form at the protein active sites during turnover and on the pathway to formation of hydrogen peroxide or water.[7,9] In a number of cases, for proteins and in synthetic inorganic systems, these exhibit diverse electronic, chemical, and physical−structural properties. The first step in dioxygen activation for cases involving O_2 addition to a single copper(I) ion involves formation of a cupric−superoxo ($Cu^{II}-O_2^{\bullet-}$) adduct (**A**) (Figure 1) which may or may not be detected.[10] This is followed by reduction−protonation by an H-atom donor, a substrate, or proton−electron sources to give a cupric−hydroperoxo product (**B**). Further protonation could

Received: June 27, 2013
Published: October 28, 2013

   dx.doi.org/10.1021/ja4065377 | J. Am. Chem. Soc. 2013, 135, 16454−16467

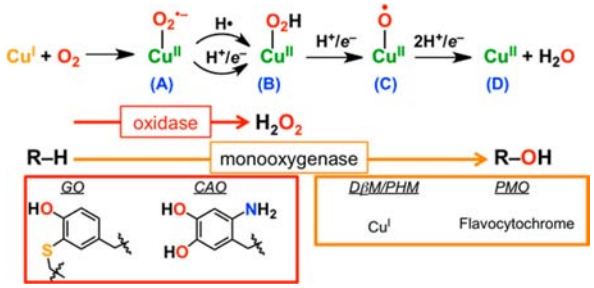

Figure 1. Copper/dioxygen intermediates and reactions catalyzed at mononuclear copper enzyme active sites. Shown in the red box are the reduced forms of the "cofactors" which provide a proton and electron for (A) → (B) in T2 copper oxidases. In the orange box is given the source of an electron involved in turnover in the copper monooxygenases DβM/PHM or PMOs. As variously proposed, this electron serves either in (A) → (B), (B) → (C), or (C) → (D).

liberate hydrogen peroxide, such as occurs in the so-called T2 oxidases, galactose oxidase (GO),[11] or copper amine oxidase (CAO)[12] (Figure 1). However, in "noncoupled" binuclear copper monooxygenases, peptidylglycine-α-hydroxylating monooxygenase (PHM), and the homologous dopamine-β-monooxygenase (DβM), further O–O reductive cleavage from the Cu^{II}–OOH entity (**B**) occurs, likely via a copper–oxyl ("cupryl") intermediate (**C**), ultimately yielding hydroxylated substrate (R–OH) and water (Figure 1). For PHM and DβM, the **A** → **B** step is postulated as that effecting H-atom abstraction from a R–H substrate,[6b,13] but other views exist.[14]

In the recently identified copper-dependent polysaccharide monooxygenases (PMOs), a single copper ion found at the enzyme active site apparently facilitates dioxygen binding and hydroxylation of cellulose by an as yet unidentified reaction mechanism.[15] By analogy to the case of PHM, a proposal for a cupric–superoxo mediated C–H activation has been mentioned.[15b]

Thus, the primary Cu^I/O_2 intermediate is the gateway complex and fundamental building block along the reductive transformation of other proposed partially reduced Cu/O_2 derived species (vide supra).[5e,16] However, the chemistry of this *initial* copper/dioxygen adduct, a Cu^{II}–$O_2^{\bullet-}$ species, is considerably less understood when compared to binuclear copper/O_2 (Cu_2O_2) complexes such as dicopper–peroxo or bis-μ-oxo adducts. The inability thus far to detect and carry out in detail studies of reactivity for biological Cu/O_2 1:1 adducts has been part of the problem. However, there is more recently a body of work where the design and synthesis of small molecule 1:1 Cu/O_2 analogues has been achieved and where ongoing efforts are intended to provide fundamental chemical insights into their structures, electronics/bonding, and reactivity. In particular, Kitajima/Fujisawa and Solomon,[17] Tolman,[18] Sundemeyer/Schindler,[19] Itoh,[20] and our own[21] research groups have significantly contributed (also see Results and Discussion), and especially of late, ligand Cu^{II}–$O_2^{\bullet-}$ complexes capable of effecting intramolecular[20a] or intermolecular[21d] C–H bond oxidations have been described.

Such chemistry is the subject of the current report. Systematic exposure of Cu^{II}–$O_2^{\bullet-}$ complexes to exogenous reductant and acid reagents has received little attention even as such reactivity could lead to Cu^{II}–OOH formation and even further transformation to yield high-valent Cu–O intermediates via subsequent O–O cleavage chemistry.[22] This approach may provide specific advantages when compared to C–H and O–H oxidation reactions including but not limited to the determination of accurate pK_a (or basicity) values and redox potentials of Cu-bound oxygen intermediates. In addition, such studies could lead to mechanistic clarification of stepwise vs concerted (H^+/e^-) reductive pathways. Herein, we report the reactivity and physical and chemical properties of an acid associated cupric superoxo complex $[(TMG_3tren)Cu^{II}(O_2^{\bullet-})(HOAc_F)]^+[B(C_6F_5)_4]^-$ (2-$B(C_6F_5)_4^-$ = $[LCu^{II}(O_2^{\bullet-})(HOAc_F)]^+$ (**2**)) reacted with electron donors. Our findings are summarized/overviewed in Figure 2. Trifluoroacetic acid

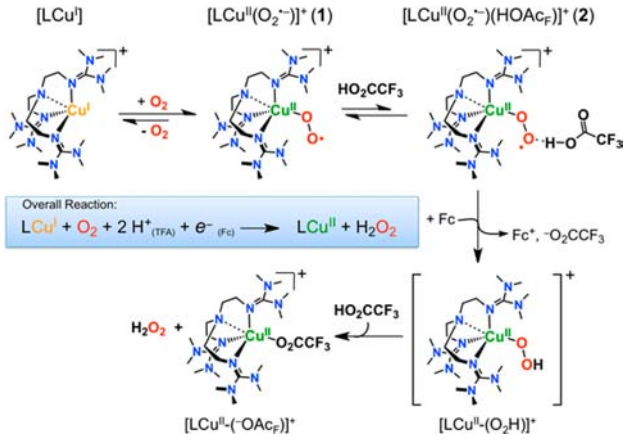

Figure 2. Reaction pathway delineated for the protonation–reduction of the cupric superoxo complex $[LCu^{II}(O_2^{\bullet-})]^+$ (**1**) by exogenous ferrocene (Fc) reductants in the presence of trifluoroacetic acid ($HOAc_F$).

($HOAc_F$) reversibly coordinates $[LCu^{II}(O_2^{\bullet-})]^+$ (**1**) to give an adduct, and only this species can undergo reduction. A cupric hydroperoxo product is implicated but it rapidly releases H_2O_2, producing a copper(II)–OAc_F complex product. The protonation equilibrium between **1** and **2** is established. The structure of the $HOAc_F$–adduct **2** is elucidated in detail, and we also describe in detail the kinetics of this complex's one-electron reduction.

2. EXPERIMENTAL SECTION

2.1. General. All materials for ligand synthesis and metal complexes were obtained from commercial sources and used as received unless stated otherwise. Inhibitor free tetrahydrofuran (THF) and 2-methyltetrahydrofuran (MeTHF) were purchased from Sigma-Aldrich and distilled under argon from sodium benzophenone prior to use. Tetrabutylammonium trifluoroacetate ($[NBu_4]^+[CF_3COO]^-$) and tetrabutylammonium BArF (=$B(C_6F_5)_4^-$) ($[NBu_4]^+[B(C_6F_5)_4]^-$) were prepared according to literature procedures.[23,24] Pentane was distilled under argon over CaH_2. Acetonitrile was stored under N_2 and purified via passage through 2 cm × 60 cm columns of activated alumina (Innovative Technologies Inc.). The synthesis of air sensitive materials was accomplished under an argon atmosphere using standard Schlenk line techniques, and the materials were stored in a MBraun glovebox with O_2 and H_2O levels at <1 ppm.

The preparation of the ligand TMG_3tren (=L) and the corresponding copper(I) BArF salt was synthesized as previously reported.[21b] TMG_3tren-d_{18} was synthesized by substituting tetramethylurea-d_6, which was synthesized according to published procedures.[25] The ^1H NMR was recorded on a Bruker 300 MHz or a Bruker 400 MHz spectrophotometer. ^2H NMR spectra were recorded on a broadband coil on a Bruker 300 MHz instrument with heteroatom nuclei resonances for ^2H and ^{19}F occurring at 46 and 282.4 MHz, respectively. Unless otherwise specified, NMR spectral peak positions were referenced against TMS or residual solvent signals. Bench-top

dx.doi.org/10.1021/ja4065377 | J. Am. Chem. Soc. 2013, 135, 16454–16467

low temperature UV−visible experiments were carried out on a Cary Bio-50 spectrophotometer equipped with an Unisoku USP-203A cryostat using a 1 cm modified Schlenk cuvette. Low temperature stopped-flow experiments were achieved using a Hi-Tech dual sequential mixing stopped-flow setup (SF-61DX2 Hi-Tech Scientific) with either a 300−700 or 300−1000 nm range diode array detector (both from Hi-Tech Scientific). Temperature control for the stopped-flow measurements was achieved by using an ethanol bath cooled by liquid nitrogen evaporation. Electrochemical experiments were performed using a BAS 100B electrochemical analyzer. EPR measurements were performed on a Bruker EMX X-band EPR spectrometer using 4 or 5 mm quartz EPR tubes. All reactions were performed in MeTHF unless specified otherwise.

2.2. Job's Plot. The total concentration of $[LCu^{II}(O_2^{\bullet-})]^+$ (**1**) + $HOAc_F$ was 3.0 mM at −130 °C. The sample was then oxygenated by bubbling O_2 for ∼30 s. After this, an appropriate amount of a 33 mM $HOAc_F$ (50−200 μL) (total volume added of LCu(I) + $HOAc_F$ = 250 μL) was added to the chilled solution and mixed by bubbling O_2 through the reaction mixture for a few seconds. The Δ-absorbance at 550 nm for the formation of $[LCu^{II}(O_2^{\bullet-})(HOAc_F)]^+$ was recorded and plotted versus mole fraction (X) copper.

2.3. Binding Constants and van't Hoff Analysis. Binding constants for the formation of $[LCu^{II}(O_2^{\bullet-})(HOAc_F)]^+$, the protonated cupric−superoxide complex, were determined in 5 °C intervals from −130 to −95 °C by the titration of a stock solution of $HOAc_F$ into a 0.17 mM solution of $[LCu^{II}(O_2^{\bullet-})]^+$. The Δ-absorbance at 448 nm corresponding to the conversion of $[LCu^{II}(O_2^{\bullet-})]^+$ to $[LCu^{II}(O_2^{\bullet-})(HOAc_F)]^+$ was equal to −0.53 AU. The equilibrium constant (K) was determined by fitting the change of absorbance at 448 nm to the following equation: $\log(\theta/(1-\theta)) = \log[HOAc_F] + \log K$ where $\theta = \Delta Abs_{448}(X)/\Delta Abs_{448}(\text{total})$. Titration data and a table with calculated equilibrium constants at each temperature employed are given in the Supporting Information.

Determination of the standard enthalpy and entropy change for the formation of $[LCu^{II}(O_2^{\bullet-})(HOAc_F)]^+$ was accomplished by van't Hoff analysis of the variable temperature titration data.

2.4. Resonance Raman (rR) Measurements. A 7 mM copper complex solution was made by dissolving 83 mg of $[LCu^{I}](B(C_6F_5)_4^-)$ in MeTHF to make a total of 10 mL solution. A 500 μL aliquot of this copper(I) solution was added to the 5 mm NMR sample tube, capped with a septum, and chilled in a pentane/$N_{2(l)}$ bath. Oxygenation of the copper samples was achieved by slowly bubbling an excess of dioxygen through the solution using a Hamilton gas-tight syringe equipped with a three-way valve and needle outlet. After addition of dioxygen, 50 μL of a 132 mM solution of $^{X}HOAc_F$ (X = 1 or 2) was added to the top of the sample tube. After 1−2 min, the solution was mixed via bubbling an additional 1 mL of dioxygen through the mixture, leading to the formation of a red solution. The final sample concentration consisted of a 6.4 mM copper and 12 mM $HOAc_F$ solution. Dioxygens, $^{16}O_2$ (Airgas OX UHP-300) and $^{18}O_2$ (Icon 6393), were added to an evacuated Schlenk flask fitted with a septum for the oxygenation reactions described above. Resonance Raman spectra were obtained using a Princeton Instruments ST-135 back-illuminated CCD detector on a Spex 1877 CP triple monochromator with 1200, 1800, and 2400 grooves/mm holographic spectrograph gratings. Laser excitation was provided by a Coherent I90C-K Kr^+ ion laser and Innova Sabre 25/7 Ar^+ ion laser with 20 mW of incident power at the sample in a ∼135° backscattering configuration. Resonance Raman spectra were collected for 10 min on a spinning sample of frozen MeTHF solutions in NMR tubes cooled to 77 K in a liquid nitrogen finger Dewar (Wilmad). For the excitation profile, the area of the 1149 cm^{-1} vibration was determined from a subtracted spectrum (spectrum of **2** prepared with $^{16}O_2$ minus the solvent spectrum). The average area was determined from three independently prepared samples, normalized to the area of a solvent vibration, by fitting a Gaussian function to the two vibrations.

2.5. X-ray Absorption Spectroscopy. A modified 10 mL Schlenk flask was charged with 5 mL of a 1 mM solution of $[LCu^{I}](B(C_6F_5)_4^-)$ and chilled to −130 °C in a pentane/$N_{2(l)}$ bath. After sample oxygenation, addition of 100 μL of a 500 mM solution of $HOAc_F$ resulted in the copper solution turning from green to a red hue. Liquid nitrogen chilled XAS sample holders were submerged into the reaction mixture, loaded, and flash frozen.

2.5.1. XAS Data Acquisition. The Cu K-edge X-ray absorption (XAS) spectra of $[LCu^{II}(O_2^{\bullet-})]^+$ (**1**) in 2-MeTHF and of **2**, formed after addition of $HOAc_F$ to **1**, were measured at the Stanford Synchrotron Radiation Lightsource (SSRL). XAS spectra of the frozen solutions in Delrin XAS cells with 37 μm Kapton windows were measured on the unfocused 20-pole, 2.0 T wiggler beamline 7-3. Storage ring parameters were 3 GeV and ∼350 mA. A Rh-coated premonochromator mirror was used for harmonic rejection and vertical collimation. A Si(220) double-crystal monochromator was used for energy selection. The samples were maintained at a constant temperature of ∼10 K during data collection using an Oxford Instruments CF 1208 continuous-flow liquid helium cryostat. A Canberra solid-state Ge 30-element array detector was used to collect Kα fluorescence. Internal energy calibration was performed by simultaneous measurement of the absorption of a Cu foil placed between two ionization chambers located after the sample. The first inflection point of the foil spectrum was assigned to 8980.3 eV. EXAFS data are reported to k = 12.85 $Å^{-1}$ in order to avoid interference from the Zn K-edge. Photoreduction was observed for both samples, as evidenced by a gradual decrease in the energy of the edge region and with slight changes in the EXAFS upon continuous scanning at the same spot. To minimize effects of photoreduction, data were collected on four physically separate spots on two sample cells for **1** and on three sample cells for **2**. The data reported here include an average of 47 scans for **1** and 12 scans for **2**.

2.5.2. XAS Data Analysis. The energy-calibrated averaged data were processed by fitting a second-order polynomial to the pre-edge region and subtracting this from the entire spectrum as a background. A three-region polynomial spline of orders 2, 3, and 3 was used to model the smoothly decaying postedge region. The data were normalized by scaling the spline function to an edge jump of 1.0 at 9000 eV. The background subtraction and normalization were done using PySpline.[26] The least-squares fitting program OPT in EXAFSPAK[27] was used to fit the data. Initial ab initio theoretical phase and amplitude functions were generated in FEFF 7.0[28] using crystallographic parameters of **1** and DFT optimized structures of **1** and **2**. During the fitting process, the bond distance (R) and the mean-square thermal and static deviations in R (σ^2) were varied for all components. The threshold energy (E_0), the point at which the photoelectron wave vector k is 0, was allowed to vary for each fit but was constrained to the same value for all components in a given fit. Coordination numbers (N) were systematically varied to evaluate chemically viable structures but were fixed within a given fit to the EXAFS data and their Fourier transform (FT).

The data for **1** show minor contamination from metallic Cu as seen from the FT peaks between 4−5 Å (Figure S12 in Supporting Information, blue line) and also evidenced during EXAFS fitting that required a peak at ∼2.6 Å (Figures S13 and S14, Table S3, fit 1B and fit 1C). This ∼2.6 Å peak can be fit with either a Cu−O/N or a Cu−Cu vector. Because of the absence of any light atom coordination around Cu at a distance of ∼2.6 Å in the crystal structure of **1**, the ∼2.6 Å peak in the data is likely from metallic Cu contamination (Figure S14 and Table S3, fit 1C). The EXAFS and FT reported here thus have a small amount (∼8%) of metallic Cu signal subtracted followed by renormalization (Figure S12, green line). EXAFS fitting of **1** before and after subtraction of Cu contamination has no significant change to the first-shell parameters. The data for **2** were collected separately and show no evidence of Cu contamination.

2.6. NMR Spectroscopy (^{2}H and ^{19}F). ^{2}H NMR experiments were performed at −120 °C using a 2.0 mM TMG_3tren-d_{18} Cu(I) ($B(C_6F_5)_4^-$) stock solution. Preparation of $[LCu^{II}(O_2^{\bullet-})]^+$ and of $[LCu^{II}(O_2^{\bullet-})(HOAc_F)]^+$ was performed at −130 °C, and the compounds were frozen in liquid nitrogen prior to insertion into the spectrophotometer. For the formation of $[LCu^{II}(O_2^{\bullet-})(HOAc_F)]^+$ the total concentration of $HOAc_F$ ($^{X}HOAc_F$ (X = 1 or 2)) was 12 mM. Using an ACD/NMR Processor Academic Edition (Advances Chemistry Development, Inc., Toronto, Ontario, Canada, www.acdlabs.com), NMR data were processed with 5 Hz line broadening

dx.doi.org/10.1021/ja4065377 | J. Am. Chem. Soc. 2013, 135, 16454−16467

applied to the FID prior to Fourier transformation. Peak positions are referenced versus the methyl signal of natural abundance deuterium in the MeTHF solvent set to 1.25 ppm.

Fluorine NMR on $[LCu^{II}(O_2^{\bullet-})(HOAc_F)]^+$ samples were performed as described above using a solvent mixture of 8:5:87 v/v (THF-d_8/α,α,α-trifluorotoluene/MeTHF) using the nondeuterated ligand supported copper complex at 5 and 12 mM $HOAc_F$. The signal corresponding to α,α,α-trifluorotoluene was set to −63.9 ppm.

2.7. EPR Spectroscopy. EPR measurements were taken at either 77 or 20 K with a total copper concentration of either 0.9 or 2.3 mM.

2.8. Hydrogen Peroxide Quantification. The spectrophotometric quantification of hydrogen peroxide was achieved by recording the intensity of the 413 nm oxidized product of diammonium 2,2′-azino-bis(3-ethylbenzothiazoline-6-sulfonate (AzBTS-$(NH_4)_2$) by horseradish peroxidase (HRP) which was adapted from published procedures. In a typical experiment 2500 μL of a 338 mM stock solution of $[LCu^I](B(C_6F_5)_4)$ was chilled to −130 °C and oxygenated for 15 s. At this time, two sample solutions of 200 μL containing ∼5 equiv of $HOAc_F$ and 1 equiv of $Me_{10}Fc$ each were added and the reaction was allowed to proceed for 1 h. Excess dioxygen was removed by performing 10 vacuum argon purge cycles at −130 °C, after which time the reaction mixture was warmed to room temperature and subjected to H_2O_2 analysis as described below. The yield of H_2O_2 is 70% in the presence of both exogenous $HOAc_F$ and $Me_{10}Fc$. In the absence of exogenous reductant (i.e., only addition of $HOAc_F$) the yield of H_2O_2 is 30%.

Hydrogen peroxide (H_2O_2) was detected using the procedure described below with the following stock solutions: 300 mM sodium phosphate buffer, pH 7.0 (solution A), 1 mg/mL AzBTS-$(NH_4)_2$ (solution B), 4 mg of HRP (type II salt free (Sigma)), and 6.5 mg of sodium azide in 50 mL of water (solution C). Quantification of hydrogen peroxide was achieved by adding a 100 μL of a MeTHF solution containing H_2O_2 to a cuvette containing 1.3 mL of water, 500 μL of solution A, and 50 μL solutions B and C. After mixing for 15 s, the samples were allowed to incubate for ∼2 min until full formation of the 413 nm band was achieved.

2.9. Electronic Structure Calculations. DFT calculations were performed using the Gaussian 09 package (revision C.01).[29] All calculations used the spin-unrestricted hybrid density functional B3LYP[30] and a mixed basis set (6-311G(d) for Cu, O, coordinated N, and the acidic H atom in $HOAc_F$, and 6-31G(d) for all other atoms) on an ultrafine integration grid. Solvation effects were accounted for using the polarized continuum model (PCM) with THF as the solvent (using default parameters). Analytical frequencies were calculated on all geometry-optimized species to verify that the species were true local minima without negative frequencies. Reported vibrational frequencies are scaled by 0.966.[31] All energies are reported as Gibbs free energies at 1 atm and 148 K (−125 °C). For time-dependent DFT calculations the first 25 roots were determined, and the calculated electronic absorption spectra were generated using SWizard[32] with 3000 cm^{-1} linewidths and Gaussian bandshapes. Wave functions were visualized with Lumo,[33] and orbital components were analyzed with QMForge.[34]

2.10. Kinetics Measurements on the Reduction of 2. Kinetics measurements on the rate of $Me_{10}Fc/Me_8Fc$ oxidation were carried out under pseudo-first-order conditions employing two experimental conditions. For condition 1, acid dependent measurements, the concentrations of $[LCu^I](B(C_6F_5)_4)$ and reductant ($Me_{10}Fc/Me_8Fc$) were fixed at 0.679 and 6.79 mM, respectively, and were prepared and transferred anaerobically to the stopped-flow instrument. Dioxygen saturated MeTHF was used for the oxygenation premixing reaction and referred to as mix 1. This solution involved in mix 1 was allowed to react at for >10 s prior to the second mixing event in order to achieve full formation of $[LCu^{II}(O_2^{\bullet-})]^+$. The $HOAc_F$ acid solutions were made in the presence of air with freshly distilled MeTHF and were discarded every 45 min and used for the second mixing event referred to as mix 2. For condition 2, reductant dependent measurements, a 0.679 mM stock solution of $[LCu^I](B(C_6F_5)_4)$ was mixed with a sample containing a varied concentration of reductant that was purged with O_2 prior to loading into the instrument. These two solutions were used in the first mixing event (mix 1). The concentration of acid stock solution was fixed at 30 mM (15 mM after dilution) $HOAc_F$ and prepared in the presence of air and discarded after every 45 min. This solution was used in the second mixing event (mix 2) in order to initiate the reaction.

Pseudo-first-order rate constants k_{obs} were determined by monitoring the decay of absorbance at 448 nm due to $[LCu^{II}(O_2^{\bullet-})]$ (**1**), which obeyed single exponential decay at >250 ms, by using the program Kinetic Studio supplied by Hi-TECH Scientific. Normalized 448 nm time dependent absorption profiles were obtained using Origin 8. Values reported for k_{obs} are the average of 10 or greater shots.

3. RESULTS AND DISCUSSION

3.1. Cupric Superoxo Complexes. As mentioned in the Introduction, the isolation of discrete cupric superoxo ($Cu^{II}-O_2^{\bullet-}$) complexes have been of considerable interest in efforts to provide chemical insight into dioxygen activation processing by copper (bio)chemical systems. In synthetic and biological systems, the lifetimes of $Cu^{II}-O_2^{\bullet-}$ adducts are dictated by multiple factors including the synthetic protocol and the ligand environment provided for the copper ion.[16a,b,35] Another major problem is that follow-up reaction of a second copper(I) precursor complex with the superoxo−copper(II) species is often faster than the initial Cu^I/O_2 binding event.[36] To date, there are three structurally reported $Cu^{II}-O_2^{\bullet-}$ complexes, as shown in Figure 3, with one example isolated in a biological setting (i.e., the enzyme PHM) and two additional structures observed using a synthetic ligand scaffold and carrying out the chemistry under cryogenic conditions.

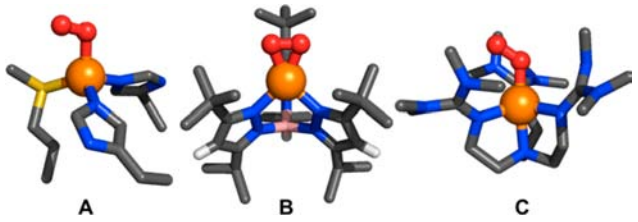

Figure 3. Crystallographically characterized Cu^{II}−superoxo complexes: (A) Cu_M site in PHM displaying $N_{(His)2}S_{(Met)}$ Cu coordination (PDB code 1SDW); (B) crystal structure of side-on cupric superoxo complex with tris-pyrazolylborate ligand displaying N_3 ligand Cu coordination (CCDC code YINBAY); (C) crystal structure of $TMG_3tren-Cu^{II}$−superoxo complex $[LCu^{II}(O_2^{\bullet-})]^+$ (**1**) displaying N_4 ligand Cu coordination (CCDC code KEKPAS).

Amzel and co-workers were able to structurally characterize a dioxygen bound form of the PHM enzyme upon dioxygen exposure of reduced enzyme crystals grown in the presence of an inhibitory substrate analogue.[7] Figure 3A is the so-called enzyme Cu_M site from the crystal structure displaying an end-on coordination mode for dioxygen to the copper metal center with ∠Cu−O−O angle of 110° and a O−O bond distance of 1.23 Å; these values are consistent with this cupric superoxide electronic configuration. There are proposals for this intermediate to directly initiate H-atom ($H^{\bullet}$) abstraction from the substrate *or* facilitate oxidation of the Cu_H site with the participation of a proton yielding a cupric hydroperoxo complex. We also note that Marletta and co-workers very recently reported the copper−oxygen intermediates observed at the active site of a copper dependent polysaccharide monooxygenase (PMO; see Figure 1). Two different species were observed, one proposed to be a cupric superoxo ($Cu^{II}-$

dx.doi.org/10.1021/ja4065377 | J. Am. Chem. Soc. 2013, 135, 16454−16467

$O_2^{\bullet-}$) moiety, the other a cupric hydroperoxo Cu^{II}–(H)OOH species.[15d]

The two synthetically derived cupric superoxo complexes shown in Figure 3B and Figure 3C exhibit different electronic and bonding geometries. The first example was reported by Kitajima, Fujisawa, and co-workers using a sterically hindered 3(*R*),5(*R*′)-disubstituted tris(pyrazolyl)borate ligand ($Tp^{R,R'}$; R = ^{t}Bu, R′ = ^{i}Pr = $Tp^{tBu,iPr}$) (Figure 3B).[17a] This Cu^{II}–$O_2^{\bullet-}$ complex binds superoxide anion in a side-on fashion and thus exhibits diamagnetic properties with an $S = 0$ ground state which is derived from the strong bonding interaction between the Cu d_{xy} and the superoxo π^*_σ orbitals. Here, the O–O bond length observed is 1.22 Å with an O–O stretching frequency of 1043 cm^{-1} ($\Delta^{18}O_2 = -59$ cm^{-1}). (Note: The latter was determined from a more sterically encumbered ligand $Tp^{Adm,iPr}$ in order to remove a binuclear, side-on peroxo contaminant.[17b]) The isoelectronic complexes, best described as side-on bound Cu(III)–peroxides (Cu^{III}–O_2^{2-}) with $\nu_{O-O} \approx 970$ cm^{-1}, have been observed by Tolman and co-workers upon dioxygen exposure to strongly donating bidentate diketiminate anionic ligand supported copper(I) species.[37]

Sundermeyer, Schindler, and co-workers reported an end-on bound superoxo copper(II) compound structure using the TMG_3tren supporting ligand (Figure 3C), $[LCu^{II}(O_2^{\bullet-})]^+$ (**1**), and this is the starting dioxygen adduct used for the chemical–spectroscopic studies described in this report.[19b] Complex **1** shows geometric properties (∠Cu–O–O = 123°; O–O = 1.28 Å) similar to those found in the PHM Cu^{II}–$O_2^{\bullet-}$ structure (vide supra). Resonance Raman spectroscopic data reveal an O–O vibration at 1120 cm^{-1} shifting to a Fermi doublet centered at 1057 cm^{-1} when **1** is formed using $^{18}O_2$.[21c] Experimental and computational evidence demonstrates that this copper(II) complex with end-on bound superoxo species has a ground state triplet electronic configuration, indicating that separate spins on the Cu(II) ion and superoxide anion reside in orthogonal orbitals.[19c,21c] $[LCu^{II}(O_2^{\bullet-})]^+$ (**1**) displays slow and limited reactivity with added phenol or catechol substrates, and over the course of reaction an internal ligand hydroxylation reaction has been observed.[21b]

3.2. Formation and Physical Properties of $[LCu^{II}(O_2^{\bullet-})(HOAc_F)]^+$ (2). As described above, the present study was initiated to elucidate aspects of the chemical reactivity of well-defined cupric–superoxo complexes but for the first time employing proton and electron sources. Initially, we examined the reaction of $[LCu^{II}(O_2^{\bullet-})]^+$ (**1**) with outer-sphere reductants. For this and other studies with copper–dioxygen complex O_2-reduction chemistries, ferrocene derivatives have been extremely useful, since a wide variety are known over a range of redox potentials and the reactions are spectroscopically convenient to monitor. However, $[LCu^{II}(O_2^{\bullet-})]^+$ (**1**) is completely unreactive to the strong reductant decamethylferrocene ($Me_{10}Fc$; $E^\circ = 0.02$ V vs SCE) and there is also no reaction even with the very powerful cobaltocene reductant ($E^\circ = -0.795$ V vs SCE).[38–39] This implies that the reduction potential of **1** must be < −0.8 V vs SCE. Thus, we turned to protonation chemistry. From initial surveys of the reactivity of $[LCu^{II}(O_2^{\bullet-})]^+$ (**1**) employing acids of differing strengths (pK_a's), we observed the formation of a new spectroscopic intermediate when utilizing trifluoroacetic acid (TFA = CF_3CO_2H = $HOAc_F$). As will be shown here, the complex formed is $[LCu^{II}(O_2^{\bullet-})(HOAc_F)]^+$ (**2**), assigned as a (**1**)/$HOAc_F$ 1:1 complex. This report will focus on the physical characterization of $[LCu^{II}(O_2^{\bullet-})(HOAc_F)]^+$ (**2**) and its chemical reactivity toward electron transfer by outer-sphere reductants.

As is already well established for a variety of solvents employed, low temperature dioxygen exposure to a solution of $[LCu^I]$ in MeTHF leads to the formation of the end-on cupric superoxide complex $[LCu^{II}(O_2^{\bullet-})]^+$ (**1**) (Figure 3C). This bright green species has a characteristic absorption spectrum as shown in Figure 4 (green spectrum) with λ_{max} = 448 (3400),

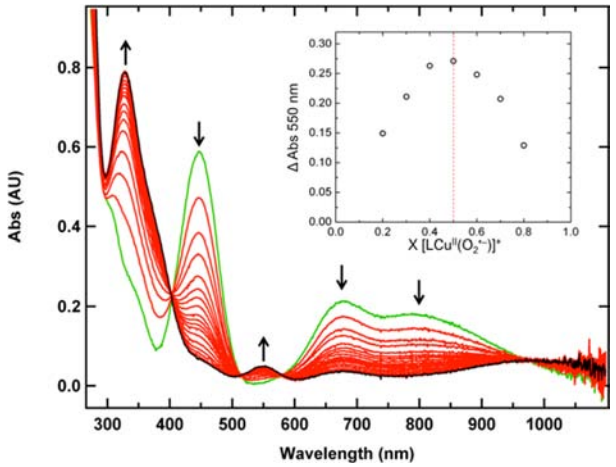

Figure 4. Conversion of $[LCu^{II}(O_2^{\bullet-})]^+$ (**1**) (green) to $[LCu^{II}(O_2^{\bullet-})(HOAc_F)]^+$ (**2**) (black) upon the addition of $HOAc_F$ at −130 °C. Insert: Job's plot for the formation of **2** that indicates a 1:1 $[LCu^{II}(O_2^{\bullet-})]^+/HOAc_F$ binding stoichiometry for the formation of **2**.

676, 795 nm [λ_{max} (ε_{max}, $M^{-1}cm^{-1}$)]. The addition of an excess of trifluoroacetic acid ($HOAc_F$) leads to the clean conversion to a new pale red metastable intermediate $[LCu^{II}(O_2^{\bullet-})(HOAc_F)]^+$ (**2**) possessing new absorption bands at 330 (5200), 382 (2600), 549 (370), 670 (170), 985 (430) nm (Figure 4 (black)). At −130 °C, **2** is stable for hours with only minimal decomposition observed as followed by either UV–vis or EPR spectroscopy.[39] The addition of an excess of triethylamine (as a base) leads to restoration of the starting **1** complex, indicating a reversible association of $HOAc_F$.[39]

The stoichiometry of $HOAc_F$ association with $[LCu^{II}(O_2^{\bullet-})]^+$ (**1**) in the formulation of $[LCu^{II}(O_2^{\bullet-})(HOAc_F)]^+$ (**2**) was obtained by Job's analysis. A maximum absorbance change at 550 nm for the formation of **2** occurs at a molar ratio of 0.5 of **1** and $HOAc_F$ as shown in the insert of Figure 4. This behavior is indicative that **2** consists of a 1:1 complex of **1** and $HOAc_F$. Spectrophotometric titration of $[LCu^{II}(O_2^{\bullet-})]^+$ (**1**) with $HOAc_F$ leads to equilibrium constants ranging from $K = 1.19 \times 10^5$ to 792 M^{-1} over the temperature range −130 to −95 °C. van't Hoff analysis of the variable temperature equilibrium constants determined for the formation of **2** is shown in the Supporting Information. The results are that for the association of $HOAc_F$ to **1**, $\Delta H^\circ = -6.9 \pm 0.7$ kcal/mol and $\Delta S^\circ = -26 \pm 4$ cal mol^{-1} K^{-1}. The large and negative value of ΔS°, in conjunction with the **1**/$HOAc_F$ 1:1 binding stoichiometry indicated by Job's analysis, suggests that liberation of superoxide ($O_2^{\bullet-}$) from the cupric center does not occur upon the association of $HOAc_F$ to $[LCu^{II}(O_2^{\bullet-})]^+$ (**1**).

3.3. Resonance Raman Spectroscopy of $[LCu^{II}(O_2^{\bullet-})(HOAc_F)]^+$ (2). Laser excitation at 368.2 nm reveals a single dioxygen isotope sensitive vibration at 1149 cm^{-1}, which shifts to 1084 cm^{-1} (Δ = 65 cm^{-1}) when $^{18}O_2$ is employed (Figure

dx.doi.org/10.1021/ja4065377 | J. Am. Chem. Soc. 2013, 135, 16454–16467

5A). The energy and isotope shift is consistent with the O−O stretch of previously characterized end-on, mononuclear

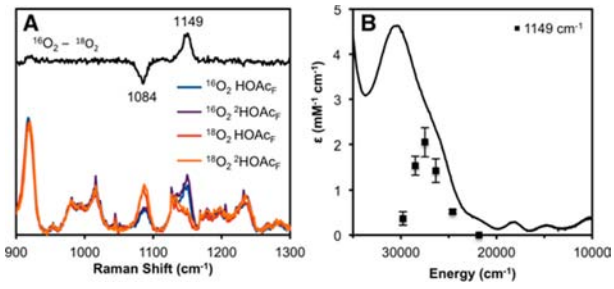

Figure 5. (A) Resonance Raman spectra of protio and deutero $[LCu^{II}(O_2^{\bullet-})(HOAc_F)]^+$ (**2**) in MeTHF collected at 77 K with 363.8 nm excitation. (B) Absorption spectrum of **2** and the relative intensity and standard deviation of the area of the 1149 cm^{-1} vibration.

copper(II) superoxide species (Table S1), including **1** (ν_{O-O} 1120 cm^{-1}; $\Delta(^{18}O_2)$ = 63 cm^{-1}). The shift in ν_{O-O} to higher energy in complex **2** relative to **1** is inconsistent with an isomerization to a side-on superoxide species, since the additional Cu−O bond results in a lower O−O frequency (~1040 cm^{-1}).[17b] From the excitation profile, the ν_{O-O} is resonance enhanced in the low energy shoulder (382 nm, 2600 M^{-1} cm^{-1}) of the intense 330 nm absorption band and is not observed in any of the other lower energy bands (Figure 5B). The significant distortion of the O−O bond in the excited state along with the energy and intensity of the 382 nm transition indicates that it is a superoxide to copper charge transfer transition. An isotope sensitive vibration corresponding to a ν_{Cu-O} is not observed in the rR spectra of **2**.

Preparation of **2** with deuterated acid (^{2}HOAc$_F$) produces a rR spectrum that is indistinguishable from **2** prepared with protio acid (Figure 5A). This suggests that the proton has not been transferred to superoxide ligand of the cupric superoxo moiety; a large deuterium isotope shift on the O−O vibration of the hydroperoxyl radical is observed in the gas phase.[40]

A comparison of the spectra of $[LCu^{II}(O_2^{\bullet-})(HOAc_F)]^+$ (**2**) to the parent compound $[LCu^{II}(O_2^{\bullet-})]^+$ (**1**) indicates that the addition of HOAc$_F$ leads to a 3860 cm^{-1} increase in the energy of the CT transition (448 to 382 nm) and an increase in the O−O stretching frequency of 29 cm^{-1}.

A similar increase in superoxide to copper CT transition (422 to 410 nm) and the O−O stretch (11 cm^{-1}) was observed between tmpa and PV-tmpa, attributed to an intramolecular hydrogen bond between the 6′-amide substituent on one of the pyridyl ligand arms of PV-tmpa and the distal oxygen of superoxide (see Figure 6).[21d,41] On the basis of these observations, a hydrogen bonding interaction to the superoxide fragment would be consistent with the increase in ν(O−O) between **1** and **2**. The change in these spectral features could

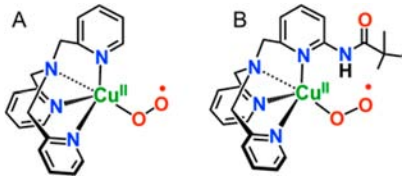

Figure 6. Ligand supported cupric superoxo complexes: (A) tmpa; (B) PV-tmpa (amide (N−H) interacts with distal O-atom).

also be attributed to differential protonation of the ligand. Both possibilities are evaluated computationally (see below).

3.4. Protonated Superoxo Complex EPR and NMR Spectroscopy. Similar to the parent superoxo complex $[LCu^{II}(O_2^{\bullet-})]^+$ (**1**), the HOAc$_F$ adduct $[LCu^{II}(O_2^{\bullet-})(HOAc_F)]^+$ (**2**) is EPR silent (X-band perpendicular mode). Further hour-long incubation of this reaction mixture at −130 °C leads to only slight decomposition, revealing a very weak nonstoichiometric typical copper(II) complex EPR signal.[39] A significant EPR signal corresponding to a full stoichiometric equivalent of the beginning sample of **2** is only observed *after* the sample is warmed to room temperature (rt).[39] The lack of *either* a Cu(II) or free superoxide EPR signal for $[LCu^{II}(O_2^{\bullet-})(HOAc_F)]^+$ (**2**) indicates it has either a singlet or triplet ground state configuration. On the basis of NMR spectroscopy (vide infra), **2** remains as possessing a triplet ground state.

We also probed possible structural rearrangements of the ligand environment upon the association of HOAc$_F$ to $[LCu^{II}(O_2^{\bullet-})]^+$ (**1**) using low temperature NMR spectroscopy employing the deuterium enriched supporting TMG$_3$tren-d_{18} ligand. This approach was applied to the study of **1** in a previous report by Roth and co-workers. In dimethylformamide (DMF) solvent at −60 °C, they observed four paramagnetically broadened methyl signals between 5 and 22 ppm. The notable paramagnetism thus suggested the triplet S = 1 electronic configuration ground state.[19c] Here, the unpaired electron on the d^9 copper(II) ion and that on the superoxide radical anion reside in orthogonal orbitals, unlike that observed in the side-on bound cupric superoxide complex studied by Kitajima/Fujisawa and Solomon where S = 0 (vide supra). This NMR splitting pattern observed by Roth suggests that in solution the three tetramethylguanidine (TMG) groups (as ligand arms) on the TMG$_3$tren ligand are symmetrically bound to the copper ion and the associated four methyl groups on each arm of the TMG group are chemically distinct. Our data essentially reproduce that observed by Roth and co-workers. We observe a very similar splitting pattern for the TMG$_3$tren-d_{18} ligand supported $[LCu^{II}(O_2^{\bullet-})]^+$ (**1**) complex in MeTHF at −120 °C as shown in Figure 7 (green). The four chemically distinct methyl signals resonate at 28.8, 22.6 (shoulder), 19.8, and 7.8 ppm.

For the trifluoroacetic acid protonated complex $[LCu^{II}(O_2^{\bullet-})(HOAc_F)]^+$ (**2**), a new chemically distinctive paramagnetically shifted ^{2}H NMR spectrum is obtained (Figure 7, red). The observed paramagnetism is inconsistent with an isomerization to a side-on superoxide species in **2**, since this

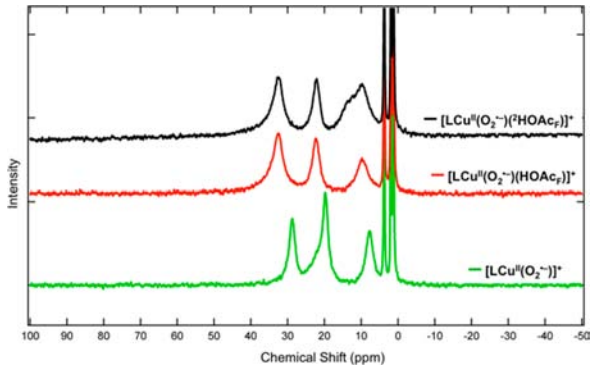

Figure 7. ^{2}H NMR spectroscopy of $[LCu^{II}(O_2^{\bullet-})]^+$ (**1**) (green), $[LCu^{II}(O_2^{\bullet-})(HOAc_F)]^+$ (**2**) (red), and $[LCu^{II}(O_2^{\bullet-})(HOAc_F)]^+$ (2-^{2}H) (black) collected at −120 °C in MeTHF. L is TMG$_3$-tren-d_{18}.

dx.doi.org/10.1021/ja4065377 | J. Am. Chem. Soc. 2013, 135, 16454−16467

species would be diamagnetic because of a stronger bonding interaction between the superoxide and the copper ion. This acid adduct possesses downfield shifted methyl signals at 32.5, 22.4, and 9.8 ppm that integrate in a ∼ 2:1:1 ratio. When deuterated acid ($^2HOAc_F$) is used in the formation of $[LCu^{II}(O_2^{\bullet-})(^2HOAc_F)]^+$ (**2**-^{2}H) the three peaks do not shift and remain in a ∼ 2:1:1 integration ratio; however, a new broad 2-H signal at ∼10.5 ppm now overlaps with the sharper 9.8 ppm resonance. We attribute this ∼10.5 signal to residual excess $^2HOAc_F$ which may be involved in dynamic exchange with **2**-^{2}H.[42] No other deuterium signals are observed for **2**-^{2}H at resonances from +600 to −35 ppm and from 0 to −300 ppm. The observed decrease in the number of chemically distinct methyl signals raises the possibility that structural rearrangement of the ligand in **2** results in a gain of symmetry upon $HOAc_F$ association with **1**; two of the four methyl groups on the N=C−$(NMe_2)_2$ moieties of each ligand arm may be chemically equivalent on the time scale of the NMR spectroscopic experiment. An alternative conclusion is that two of the four $-CD_3$ resonances happen to have coinciding chemical shifts. The very similar paramagnetic shifts displayed by the ligand in the ^{2}H NMR experiments for $[LCu^{II}(O_2^{\bullet-})(HOAc_F)]^+$ (**2**) and $[LCu^{II}(O_2^{\bullet-})]^+$ (**1**) suggest a common triplet electronic ground state. This is consistent with the lack of an observed X-band EPR signal for both complexes (*vide supra*).

The question of proximity of the trifluoroacetic acid molecule with respect to the paramagnetic $Cu^{II}-O_2^{\bullet-}$ core was also probed via low temperature ^{19}F NMR spectroscopy. The addition of $HOAc_F$ to $[LCu^{II}(O_2^{\bullet-})]^+$ (**1**) at −120 °C leads to a new thermally sensitive broad and chemically distinct fluorine signal occurring at −83.0 ppm attributed to the $HOAc_F$ molecule associated with $[LCu^{II}(O_2^{\bullet-})(HOAc_F)]^+$ (**2**) (see Figure 8). Integration of the −83.0 ppm signal in comparison

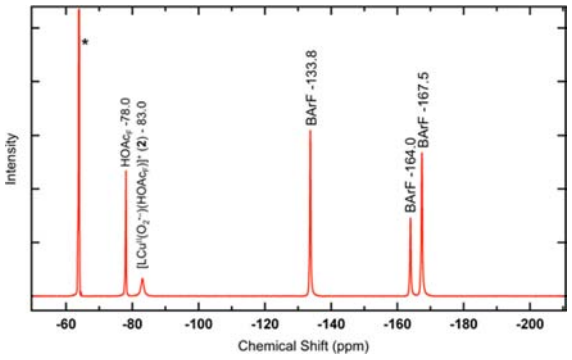

Figure 8. ^{19}F NMR spectrum of $[LCu^{II}(O_2^{\bullet-})(HOAc_F)]^+$ (**2**) collected at −120 °C. The paramagnetically broadened signal resonating at −83.0 ppm is attributed to $HOAc_F$ in complex **2**. Also observed in this spectrum is residual (nonassocated) $HOAc_F$ at −78.0 ppm and three fluorine signals associated with the BArF ($B(C_6F_5)_4^-$) anion resonating at −133.8, −164.0, and −167.5 ppm. All chemical shifts are referenced vs $CF_3C_6H_5$ (*) set to −63.9 ppm.

to the para-fluorine of the $B(C_6F_5)_4^-$ counteranion as an internal standard indicates this adduct **2** is generated in ∼80% yield. This stoichiometry is consistent with a 1:1 formulation of **1**/$HOAc_F$ of **2** as indicated by Job's plot analysis and provides evidence against formulations involving multiple equivalents of $HOAc_F$. Also observed in this spectrum is residual excess $HOAc_F$ resonating at −78 ppm, in which the chemical shift appears to be unaffected by the presence of **2**. It is notable that the −83 ppm ^{19}F signal is broadened compared to the nonassociated excess $HOAc_F$ and also compared to the fluorine atom resonances in $B(C_6F_5)_4^-$. This behavior further supports the premise that the $HOAc_F$ molecule associated with **2** is in proximity to the paramagnetic triplet $Cu^{II}-O_2^{\bullet-}$ core. Additional experiments of interest include the finding that the addition of $[NBu_4]^+[OAc_F]^-$ to $[LCu^{II}(O_2^{\bullet-})]^+$ (**1**) does not lead to formation of the −83 ppm signal, clearly demonstrating that this signal is distinct from free $^-OAc_F$ anion under these condition.[43]

In summary, the low-temperature ^{2}H and ^{19}F NMR spectroscopic experiments on $[LCu^{II}(O_2^{\bullet-})(HOAc_F)]^+$ (**2**) support the formulation for **2** and that it is a paramagnetic 1:1 adduct of $HOAc_F$ and $[LCu^{II}(O_2^{\bullet-})]^+$ (**1**). The experiments with the deuterium enriched ligand supported complex suggest a small structural rearrangement of the TMG_3tren ligand arms upon association of $HOAc_F$. Fluorine NMR spectroscopy suggests a proximity of $HOAc_F$ to the $Cu^{II}-O_2^{\bullet-}$ core. While the rR spectroscopic data implicate an acid with superoxide ligand interaction, the combined data do not address whether or not the $HOAc_F$ molecule has undergone dissociation via proton transfer to the ligand in **2**. Thus, we turned to XAS and DFT calculations to provide further insights into (i) the structural rearrangements occurring upon $HOAc_F$ association with the cupric superoxide complex **1** and (ii) the electronic structural properties of $[LCu^{II}(O_2^{\bullet-})(HOAc_F)]^+$ (**2**).

3.5. XAS. Cu XANES. The Cu K-edge XAS spectra for $[LCu^{II}(O_2^{\bullet-})]^+$ (**1**) (green line) and $[LCu^{II}(O_2^{\bullet-})(HOAc_F)]^+$ (**2**) (red line) are shown in Figure 9. The second derivative of

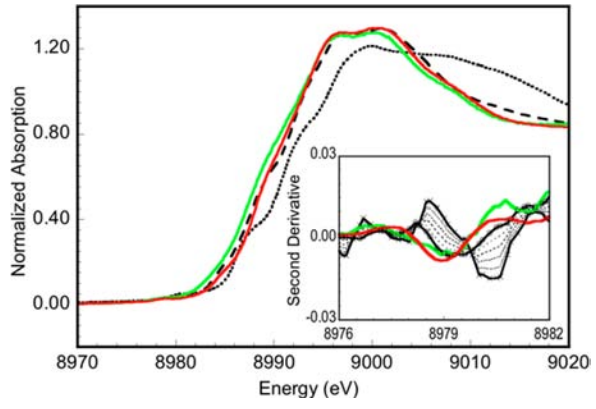

Figure 9. Cu K-edge XAS spectra of **1** (green line), **2** (red line), and model ($[Cu^{II}(HB(3,5\text{-}Ph_2pz)_3)]_2(O_2)$) (---/○) and $[Cu^{III}_2(TACN^{Bn3})_2(O_2)]^{2+}$ (···/×) complexes. (Inset) Smoothed second derivative of the pre-edge region with simulated spectra generated with the following ratios of the Cu(II) and Cu(III) models: 80:20, 60:40, 40:60, and 20:80 (···).

the data is shown in the inset that reveals a 1s → 3d pre-edge transition at ∼8979 eV for both samples. The energy of this transition is characteristic of Cu(II). Conversely, Cu(III) species exhibit a pre-edge shift of ∼1.0−2.0 eV to higher energy relative to analogous Cu(II) complexes.[44] Figure 9 also includes previously studied models, $[Cu^{II}(HB(3,5\text{-}Ph_2pz)_3)]_2(O_2)$ and $[Cu^{III}_2(TACN^{Bn3})_2(O_2)]^{2+}$ as references.[45] The data show that **2** has no observable feature between 8980 and 8981 eV that would be attributed to the presence of Cu(III).

3.6. Cu EXAFS. The k^3-weighted EXAFS data and their FT of $[LCu^{II}(O_2^{\bullet-})]^+$ (**1**) (green line) and $[LCu^{II}(O_2^{\bullet-})$-

dx.doi.org/10.1021/ja4065377 | J. Am. Chem. Soc. 2013, 135, 16454−16467

$(HOAc_F)]^+$ (**2**) (red line) are shown in Figure 10. The EXAFS fit parameters of **1** and **2** are given in Table 1 (EXAFS fits are given in Figures S15 and S16). The first-shell EXAFS data of **1** were best fit with one Cu−O/N at 1.93 Å and four Cu−N/O at 2.10 Å (fit 1A). These distances well reproduce the crystallographic distances (Cu−O = 1.93 Å and average of the four Cu−N = 2.10 Å) of this complex **1**.[19b] The major change observed in the data in converting **1** to **2** via $HOAc_F$ association is an increase in the EXAFS and FT intensities. A good fit to the data was again achieved with a split first shell with one Cu−O/N at 1.94 Å and four Cu−N/O at 2.08 Å (fit 2A) with smaller σ^2 values than those observed for **1** or with one Cu−O/N at 1.93 Å and five Cu−N/O at 2.08 Å (fit 2B, Table S4) with similar σ^2 values as for **1** (see Table 1). Thus, the increased intensity in **2** is accounted for by either a coordination number of 5 with smaller σ^2 values or a coordination of 6 with larger σ^2 values. However, a six-coordinate Cu(II) complex with six Cu−N/O distances less than 2.1 Å is inconsistent with Cu(II) complexes undergoing a Jahn−Teller distortion, which would result in at least two Cu−N/O distances of ≥2.1 Å. Therefore, we disfavor this interpretation and conclude that **2** must be five-coordinate.

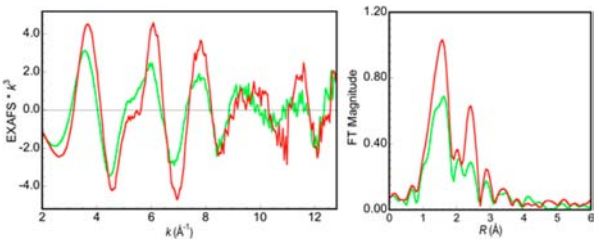

Figure 10. Cu K-edge EXAFS data (left) and non-phase-shift-corrected FT (right) of **1** (green line) and **2** (red line). Phase shift in the first shell is ∼0.4 Å.

Small changes in the first-shell distances were observed for different spline functions used for data reduction, giving an error of ±0.05 Å for both species. Other first-shell fits with a combination of two to four short and one to three long Cu−O/N bonds were also attempted for both **1** and **2**. These fits were not justified because of higher error function or small σ^2 values (<0.000 50) or because the split in distance between the two first-shell paths was less than the allowed resolution of the data (0.14 Å). The FT peaks in the R = 2.0−2.8 Å range for both **1** and **2** were fit using single scattering (SS) and multiple scattering (MS) contributions from the alkyl backbone of the ethylamine. The peaks in the R = 2.8−4.0 Å range were fit with SS contributions from the guanidino amino and methyl groups.

Altogether, the rR, NMR, and XANES/EXAFS comparisons of $[LCu^{II}(O_2^{\bullet-})]^+$ (**1**) and $[LCu^{II}(O_2^{\bullet-})(HOAc_F)]^+$ (**2**) indicate that the coordination geometries, i.e., the number of ligands and their arrangement, are essentially unchanged upon addition of $HOAc_F$ to **1**. As indicated, large differences in electronic structure have been revealed based the significant shifts in the $O_2^{\bullet-}$ → Cu charge transfer band energy and O−O stretching frequency (vide supra).

3.7. DFT Models of 2. Density functional theory calculations were performed on $[LCu^{II}(O_2^{\bullet-})]^+$ (**1**) and several possible structural isomers of $[LCu^{II}(O_2^{\bullet-})(HOAc_F)]^+$ (**2**) to identify a plausible site of protonation. From the experimental data, these structural models were restricted to a 1:1 Cu/$HOAc_F$ stoichiometry as indicated by the Job's plot experimental results (see Figure 4; vide supra) and with a triplet (S = 1) ground state. Four of the candidate models of **2** (Figure 11) differed by the site of protonation: NMe_2 (model **2A**), a coordinating imine (**2B**, with $^-OAc_F$ occupying the vacant coordination site), the distal oxygen atom of the superoxo (**2C**), or the tripodal tertiary amine (**2E**). Finally, we also considered formation of a 1:1 Cu/$HOAc_F$ adduct without proton transfer (**2D**).[46] The calculated ν_{O-O} frequencies, relevant bond lengths, and free energies (relative to **1** + $HOAc_F$) for these models are given in Table 2, and TD-DFT calculated UV−vis absorption spectra of **1** and the three lowest-energy models of **2** are shown in Figure 12.

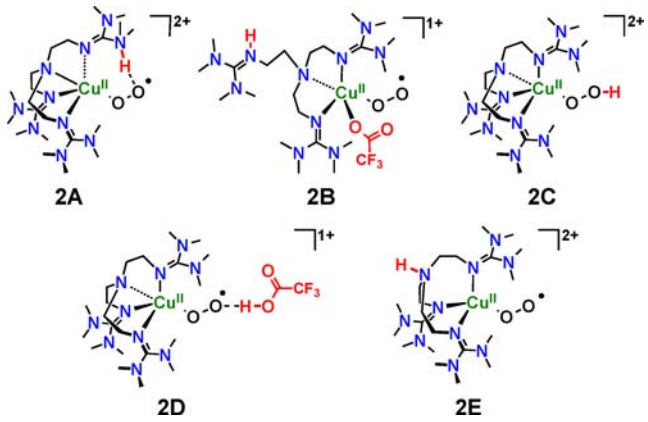

Figure 11. (Left) Isomers of complex **2** analyzed by DFT.

Table 1. EXAFS Least-Squares Fitting Results for k = 2−12.85 Å^{-1} for 1 (Left) and 2 (Right)

species **1**		fit 1A		species **2**		fit 2A	
coord no.	path	R (Å)[a]	σ^2 (Å^2)[b]	coord no.	path	R (Å)[a]	σ^2 (Å^2)[b]
1	Cu−O/N	1.93	399	1	Cu−O/N	1.94	130
4	Cu−N/O	2.10	492	4	Cu−N/O	2.08	335
6	Cu−C	2.87	921	6	Cu−C	2.89	379
12	Cu−N−C	3.24	520	12	Cu−N−C[d]	3.22	379
6	Cu−C	3.89	572	3	Cu−C	3.46	1005
6	Cu−N	4.05	843	6	Cu−N	3.90	1014
E_a (eV)		−8.01		E_a (eV)		−4.67	
F[c]		0.16		F[c]		0.20	

[a]The estimated standard deviations in R for each fit is ±0.02 Å. [b]The σ^2 values are multiplied by 10^5. [c]The error F is given by $\sum[(\chi_{obsd} - \chi_{calcd})^2k^6]/\sum[(\chi_{obsd})^2k^6]$. [d]$\sigma^2$ for the multiple scattering path is linked to the corresponding single scattering path.

dx.doi.org/10.1021/ja4065377 | J. Am. Chem. Soc. 2013, 135, 16454−16467

Table 2. Selected Geometric, Vibrational, and Free Energy Data for DFT-Calculated Species 1 and 2A−E

	ΔG_{rel} [a]	ν_{O-O} ($\Delta\nu_{180}$) [$\Delta\nu_{2H}$][b] (cm^{-1})	r_{O-O} (Å)	r_{Cu-O} (Å)	∠Cu−O−O (deg)	$r_{Cu\text{-}ligand}$ (Å)[c]
1	0	1172 (−73)	1.298	1.952	120.7	2.154; 2.112/2.142/2.163
2A	+8.2	1186 (−68) [−0.2]	1.307	1.962	118.0	2.099; 2.005/2.007/2.635
2B	−10.4	1177 (−73) [0]	1.292	1.974	120.3	2.270; 1.993/2.230; 2.054
2C	+20.4	1060 (−61) [−11.3]	1.340	2.030	121.0	2.060; 2.056/2.082/2.145
2D	−7.1	1189 (−71) [−0.3]	1.309	1.958	119.6	2.114; 2.109/2.134/2.146
2E	+21.0	1183 (−66) [0]	1.287	1.938	98.3	3.549; 2.032/2.067/2.124

[a]Free energy in kcal/mol at 148 K (−125 °C) relative to **1** + $HOAc_F$. The outer-sphere $^-OAc_F$ anion was included in computational models **2A**, **2C**, and **2E** for the determination of ΔG_{rel}. [b]Calculated shift in the $^{16}O-^{16}O$ stretching frequency in the presence of $^2HOAc_F$. [c]The Cu−N_{amine} distance is listed first followed by the Cu−N_{imine} distances. For **2B**, the Cu−O_{Ac} distance is listed last.

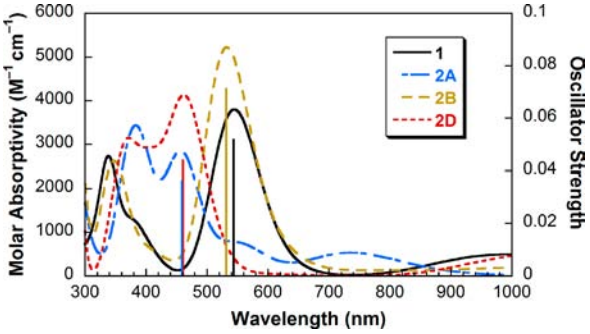

Figure 12. TD-DFT calculated UV−vis absorption spectra for **1**, **2A**, **2B**, and **2D**. For each species, the calculated energy and oscillator strength of the O_2 → Cu LMCT is indicated with a vertical bar.

Structure **2C** with a protonated superoxo can be immediately excluded as a candidate model, since the calculated wave function has significant Cu^{3+} character (inconsistent with Cu^{2+} in the XAS pre-edge) and a much lower ν_{O-O} frequency than $[LCu^{II}(O_2^{\bullet-})]^+$ (**1**), inconsistent with the +29 cm^{-1} increase observed by rRaman spectroscopy on $[LCu^{II}(O_2^{\bullet-})(HOAc_F)]^+$ (**2**). Furthermore, the presence of an O−H bond requires a sizable $^1H/^2H$ isotope effect on ν_{O-O} (calcd $\nu_{O-O(H)} - \nu_{O-O(D)}$ = −11.3 cm^{-1}), but no isotope-sensitive features were observed in the reaction of **1** with $^1HOAc_F/^2HOAc_F$ (see Figure 5). Although the protonated imine structure **2B** is exergonic with respect to **1** + $HOAc_F$, it does not reproduce the large change in ν_{O-O} frequency (calcd +3 cm^{-1}) and LMCT energy (calcd +400 cm^{-1}) that is observed for **2** (obsd +29 and 3860 cm^{-1}). Therefore, we also rule out structure **2B**. Models **2A** and **2D** that include the acidic H-atom hydrogen-bonded to the superoxo each reproduce the shift in ν_{O-O} to higher frequency (calcd +14 and +17 cm^{-1}, respectively) and LMCT to higher energy (both calcd +3300 cm^{-1}). Additionally, there is a minimal calculated $^1H/^2H$ isotope effect on ν_{O-O} (<0.3 cm^{-1}) for both **2A** and **2D**, consistent with identical rR spectra obtained with $^1HOAc_F$ and $^2HOAc_F$. However, model **2A** has a pseudo-four-coordinate geometry with a very long axial Cu···N_{imine} distance of >2.6 Å, which is inconsistent with the coordination number ≥5 that is required to fit the EXAFS data. Therefore, *model **2D** is the only model that reproduces the combined spectroscopic data,* including the 5-coordinate EXAFS fit, the significant shift of both ν_{O-O} and LMCT to higher energy, and lack of an $^1H/^2H$ isotope effect on ν_{O-O}. Model **2D** is also consistent with the ^2H and ^{19}F NMR spectroscopic data for **2**. Assuming rapid precession around the Cu−O bond in solution (which also must be present in **1**), **2D** would be expected to exhibit 3-fold symmetry in its ^2H NMR spectrum, and the proximity of $HOAc_F$ to the paramagnetic core would explain the broad resonance in the ^{19}F NMR spectrum. Finally, model **2D** is calculated to be both exothermic and exergonic from **1** and $HOAc_F$ at −125 °C (ΔH^o = −11.9 kcal/mol; $\Delta G_{-125°C}$ = −7.1 kcal/mol), with results similar in magnitude to the experimentally determined values of ΔH^o = −6.9 kcal/mol and $\Delta G_{-125°C}$ = −3.8 kcal/mol.

3.8. Effect of $HOAc_F$ on the ν_{O-O} Frequency and LMCT Energy. Consistent with the experimental data, structure **2D** predicts a shift in ν_{O-O} to a higher frequency than in $[LCu^{II}(O_2^{\bullet-})]^+$ (**1**). However, the DFT model also predicts a longer O−O bond in **2D** than in **1** (1.309 vs 1.298 Å, respectively), which would be expected to result in a *lower* energy ν_{O-O} due to a weaker bond. To resolve this discrepancy, we investigated the effect of the $HOAc_F$ dipole on the geometry and electronic structure of the Cu−$O_2^{\bullet-}$ fragment. First, by use of the molecular coordinates of the Cu−$O_2^{\bullet-}$ fragment in **2D** with $HOAc_F$ removed, ν_{O-O} was calculated to be 1129 cm^{-1} (i.e., 43 cm^{-1} lower than **1**), as would be expected from its longer O−O bond. Next, we examined a modified model of **2D** where the atoms of $HOAc_F$ were replaced by point charges in order to mimic the electrostatic effect of the $HOAc_F$ dipole without introducing covalent ffects of the hydrogen bond.[47] In the presence of the $HOAc_F$ dipole, ν_{O-O} shifted to 1180 cm^{-1} (i.e., 51 cm^{-1} higher than without the dipole), which is close to that observed for the full model **2D** (1189 cm^{-1}). Thus, the shift to a higher frequency ν_{O-O} in **2** results from an electrostatic interaction between $HOAc_F$ and the copper superoxide.

The increase in ν_{O-O} frequency is rationalized by the antiparallel orientation of the $HOAc_F$ and O_2 dipoles (Figure 13A); stretching the O−O bond results in an increased O−O dipole that is aligned opposite the $HOAc_F$ dipole, resulting in a net higher frequency ν_{O-O}. The weaker O−O bond in **2** results from an increase in the amount of filled π^*_σ antibonding character upon binding $HOAc_F$. In **2**, the occupied β-MOs (Figure S18) account for 84% of the total π^*_σ character (the remaining 16% is mixed with the Cu d_{z^2} in the β-LUMO), compared to 74% π^*_σ in occupied β-MOs in **1** (26% π^*_σ in the unoccupied Cu d_{z^2}). Together, these results confirm that the O−O bond *is* weaker in **2**, yet the observed higher ν_{O-O} frequency is due to the presence of the $HOAc_F$ dipole that causes a shift to higher energy, dominating the opposing shift to lower energy due to the change in geometry.

The blue shift in the $O_2^{\bullet-}$ → Cu CT transition in the UV−vis absorption spectrum of $[LCu^{II}(O_2^{\bullet-})(HOAc_F)]^+$ (**2**) (see Figure 4 and Supporting Information) can also be explained by the presence of the $HOAc_F$ dipole in proximity to the Cu−O_2 core. TD-DFT calculations on the "dipole only" form of **2D** indicate that the key O_2 (π^*_σ) → Cu (d_{z^2}) charge transfer increases by ∼2200 cm^{-1} when the $HOAc_F$ dipole is included

dx.doi.org/10.1021/ja4065377 | J. Am. Chem. Soc. 2013, 135, 16454−16467

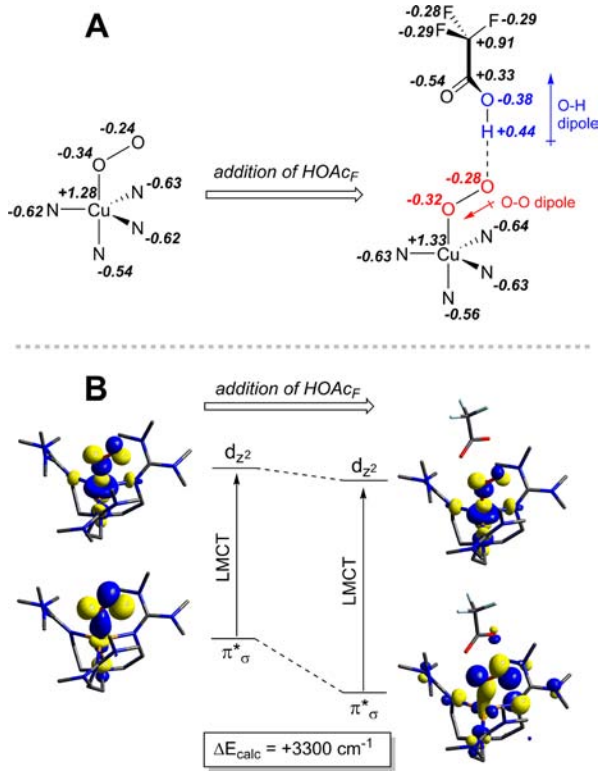

Figure 13. (A) Mulliken charges of core atoms in DFT models of **1** (left) and **2D** (right). Note that the O−O and O−H dipoles are oriented in opposite directions. (B) Effect of $HOAc_F$ on calculated LMCT energy. The donor and acceptor states for the LMCT have predominantly π^*_σ and d_{z^2} character, respectively. The corresponding β-spin orbitals of π^*_σ and d_{z^2} character are visualized for **1** (left) and **2D** (right). Orbital contours are plotted with an isovalue of 0.05.

in the model. This is perhaps not surprising, since the $HOAc_F$ dipole will have a larger electrostatic stabilization of the doubly occupied $O_2^{\bullet-}$ π^*_σ (the LMCT donor MO) than the singly occupied Cu d_{z^2} (LMCT acceptor orbital) due to the proximity of the positive end of the dipole to the $O_2^{\bullet-}$ moiety, resulting in an increase of the donor/acceptor orbital splitting and a higher energy LMCT (Figure 13B).

In summary, these results indicate that the trifluoroacetate remains protonated and hydrogen-bonds to the distal oxygen of the superoxo fragment in $[LCu^{II}(O_2^{\bullet-})(HOAc_F)]^+$ (**2**). The spectroscopic features displayed by **2** are a result of the electrostatic interaction with the dipole of $HOAc_F$ and not a change in orbital covalency imparted by the hydrogen bond.

3.9. Reactivity of $[LCu^{II}(O_2^{\bullet-})(HOAc_F)]^+$ (2) toward Exogenous Substrates. A facile electron transfer is observed upon the addition of the exogenous electron donors $Me_{10}Fc$ (E_{ox} = 0.020 V vs SCE) and Me_8Fc (E_{ox} = 0.120 V vs SCE) to complex **2**, yielding 1 equiv of oxidized ferrocenium ion, $Me_{10}Fc^+$ and Me_8Fc^+, respectively. This reactivity is in stark contrast to that of the parent $[LCu^{II}(O_2^{\bullet-})]^+$ (**1**), in which no electron transfer was observed with Me_8Fc, $Me_{10}Fc$, or even cobaltocene (vide supra). Reactivity studies performed at −130 °C on **2** with an excess of exogenous substrates including thioanisole, 2,6-di-*tert*-butyl-4-methoxyphenol, and 9,10-dihydro-10-methylacridine lead to little to no change in the optical spectrum. A lack of exogenous C−H, O−H, and oxo transfer reactions between **2** and substrates may have to do with its inherent reaction properties, or it could be that the associated $HOAc_F$ molecule limits access and approach of the substrate to the $Cu^{II}-O_2^{\bullet-}$ core.

In the electron-transfer reactions of **2** with $Me_{10}Fc$ and Me_8Fc, the overall chemistry is highlighted in Figure 2. While it requires excess $HOAc_F$ to fully form $[LCu^{II}(O_2^{\bullet-})(HOAc_F)]^+$ (**2**) (vide supra), the overall stoichiometry requires the addition of 2 equiv of $HOAc_F$ and 1 equiv of $Me_8Fc/Me_{10}Fc$ to the $[LCu^{II}(O_2^{\bullet-})]^+$ (**1**) complex to yield 1 equiv of hydrogen peroxide (H_2O_2), 1 equiv of oxidized ferrocene ($Me_8Fc^+/Me_{10}Fc^+$), and a $[LCu^{II}(OAc_F)]^+$ product complex (Figure 2). Experiments where the amount of reductant was varied indicate that only 1 equiv is required.[39] When only 1 equiv of acid is employed in the presence of excess reductant, the reaction only proceeds halfway.[39] We can conclude that when $[LCu^{II}(OOH)]^+$ forms, it undergoes protonation more efficiently than does occur ferrocenyl reduction of $[LCu^{II}(O_2^{\bullet-})(HOAc_F)]^+$ (**2**) (see Figure 2). Thus, one-half of the added 1 equiv acid produces $[LCu^{II}(OOH)]^+$ while the other half protonates the latter to give H_2O_2 and $[LCu^{II}(OAc_F)]^+$. This cupric−trifluoroacetate complex was identified by EPR spectroscopy, in comparison to an "authentic" sample generated by addition of a stoichiometric amount of $AgOAc_F$ to $[LCu^{II}(Cl)]^+$.[39] Quantitation of the H_2O_2 formed (when a small excess of acid was employed) led to a 70% yield (see Experimental Section).

3.10. Kinetics of the Ferrocenyl Reduction of $[LCu^{II}(O_2^{\bullet-})(HOAc_F)]^+$ (2). As described and demonstrated below, **2** is reduced by ferrocenyl derivatives in an overall second-order process, with a first-order dependence on both **2** and Me_8Fc (or $Me_{10}Fc$). The formation of complex **2** under the conditions employed (−80 °C) is related to complex **1** via a rapid $HOAc_F$ equilibrium-binding event. The disappearance of **1** (and thus **2**) at −80 °C in the presence of excess reductant (Me_8Fc and $Me_{10}Fc$) obeys a first-order decay model.[39] Thus, the overall kinetics are described by a rapid preequilibrium (K_{HOAcF}) followed by the irreversible and rate-limiting ferrocenyl electron transfer reduction event (k_{et}), eqs 1 and 2. Equations 3 and 4 describe the overall kinetic process.

$$\mathbf{1} + HOAc_F \rightleftharpoons \mathbf{2} \qquad (K_{HOAcF}) \tag{1}$$

$$\mathbf{2} + Fc \rightarrow \text{products} \quad (k_{et}) \text{ rds} \tag{2}$$

$$d[\text{products}]/dt = k_{et}[\mathbf{2}][Fc] = k_{obs}[\mathbf{1}] \tag{3}$$

$$k_{obs} = (k_{et}K_{HOAcF}[HOAc_F][Fc])/(1 + K_{HOAcF}[HOAc_F]) \tag{4}$$

The determination of the kinetics of $[LCu^{II}(O_2^{\bullet-})(HOAc_F)]^+$ (**2**) promoted ferrocenyl electron transfer was achieved by examining the loss of $[LCu^{II}(O_2^{\bullet-})]^+$ (**1**) under two separate experimental conditions. The concentrations of $HOAc_F$ and ferrocene reductant were systematically and independently varied. Each reaction condition displays different kinetics behavior with respect to the concentration of varied substrate. As stated above, **2** is rapidly formed at −80 °C, being observed in the first spectrum (collected at t = 1.5 ms) after the introduction of acid to **1** with the initial amounts of **1** and **2** observed being dependent on the concentration of $HOAc_F$ employed.[39] Thus, the rate constant for association of $HOAc_F$ to **1** (k_1) is very much larger than k_{et}, and k_{et} is associated with the rate-determining step. However, as the adduct **2** is responsible for ferrocenyl oxidation and is formed in a nonlinear fashion with respect to increasing $HOAc_F$ concen-

dx.doi.org/10.1021/ja4065377 | J. Am. Chem. Soc. 2013, 135, 16454−16467

tration (K_{HOAcF} = 165 ± 90 M^{-1} at −80 °C), k_{obs} will display similar behavior with respect to $HOAc_F$ until a maximum rate (k_{obs}) is observed, i.e., saturation behavior (Figure 14A).

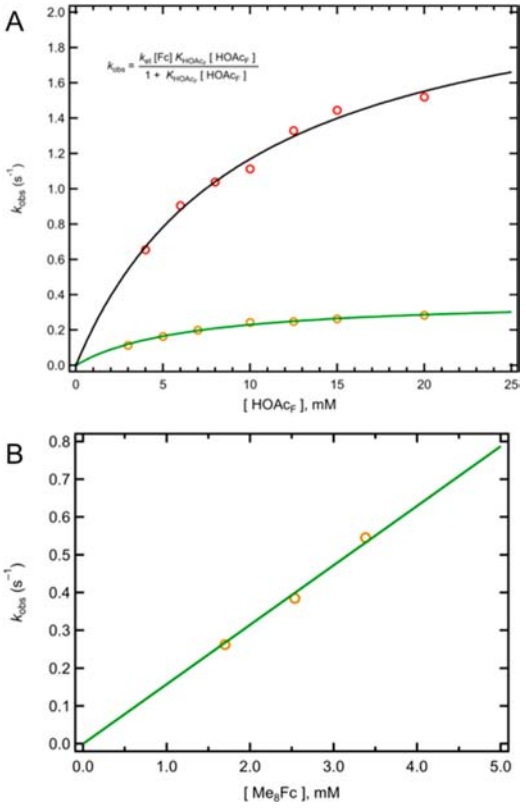

Figure 14. (A) First-order decomposition rate constants for the disappearance of $[LCu^{II}(O_2^{\bullet-})]^+$ (**1**) observed at 448 nm with 1.69 mM (10 equiv) reductant $Me_{10}Fc$ (red circles) and Me_8Fc (gold circles) at −80 °C as a function of increasing concentrations of $HOAc_F$. Black and green lines are the linear fits for the $Me_{10}Fc$ and Me_8Fc respective k_{obs} values according to eq 4. Extrapolation for the second-order rate constant (k_{et}) of 1365 ± 75 and 225 ± 8 M^{-1} s^{-1} for the oxidation of $Me_{10}Fc$ and Me_8Fc, respectively, by $[LCu^{II}(O_2^{\bullet-})(HOAc_F)]^+$ (**2**) is obtained. (B) First-order rate constants for the disappearance of $[LCu^{II}(O_2^{\bullet-})]^+$ (**1**) followed at 448 nm at 15 mM $HOAc_F$ as a function of increasing concentration of the reductant Me_8Fc (10−20 equiv vs **1**). A slope and thus a second-order rate constant of 158 ± 3 M^{-1} s^{-1} is obtained. See text.

The kinetic behavior just described applies to both Me_8Fc and $Me_{10}Fc$ as reductants. The largest reaction rate observed in the two cases are not equal, displaying a maximum value of k_{obs} as 0.38 and 2.36 s^{-1}, respectively, for Me_8Fc and $Me_{10}Fc$ when k_{obs} is modeled using eq 4 and is shown in Figure 14A. These results indicate that the rate-determining step contains a redox component, as the stronger reductant $Me_{10}Fc$ can more rapidly reduce $[LCu^{II}(O_2^{\bullet-})(HOAc_F)]^+$ (**2**) when compared to Me_8Fc. These saturation values of k_{obs} lead to an estimation of the second-order electron transfer rate constant (k_{et}) of 225 ± 8 and 1365 ± 75 M^{-1} s^{-1} for the oxidation of Me_8Fc and $Me_{10}Fc$, respectively, by **2**. Equation 4 also allows for an estimate of the equilibrium constant for K_{HOAcF} of 154 ± 15 (from the Me_8Fc data) and 103 ± 13 M^{-1} (from the $Me_{10}Fc$ data) for the redox reactions which are in reasonable agreement with the value of 165 ± 90 M^{-1} obtained from van't Hoff analysis at this temperature (−80 °C) (see above). Along these lines, the much weaker reductant dimethylferrocene (Me_2Fc; $E°$ = 0.435 vs SCE) does not lead to any observable oxidized ferrocenium products, thus bracketing the reduction potential of **2** between 0.120 and 0.435 V vs SCE (not accounting for solvent or temperature effects). Note that this is very different from the reduction potential of **1** (<−0.8 V vs SCE), which highlights the substantial effect of hydrogen-bonded $HOAc_F$ on reduction potential, even without proton transfer.

Further, this affect is consistent with DFT calculations, which predict that association of $HOAc_F$ leads to spontaneous transfer of the proton upon one-electron reduction, which increases the electron affinity by ∼1.1 eV (see Supporting Information). Thus, the hydrogen-bonded $HOAc_F$ provides an extra 25 kcal/mol driving force for substrate (ferrocenyl reductant) oxidation by **2** relative to **1** through a PCET process.

We were also able to investigate the effects of varying reductant concentrations on k_{obs} at a fixed concentration of $HOAc_F$ (i.e., 15 mM). With this large amount of acid, the predominant copper species present in solution is $[LCu^{II}(O_2^{\bullet-})(HOAc_F)]^+$ (**2**). Thus, the kinetics situation will more accurately represent that predicted by eqs 3 and 4. Figure 14B displays results of such experiments, demonstrating a linear correlation with respect to reductant concentration, revealing a second-order rate constant of 158 ± 3 M^{-1} s^{-1} compared to the value of 225 ± 8 M^{-1} s^{-1} (see above). This behavior is consistent with a reaction mechanism involving rate-determining electron transfer with a transition state comprising a 1:1 stoichiometry of $[LCu^{II}(O_2^{\bullet-})(HOAc_F)]^+$ and Me_8Fc.

4. FURTHER REMARKS AND CONCLUSIONS

The kinetics investigation into the oxidation of ferrocenes by $[LCu^{II}(O_2^{\bullet-})]^+$ (**1**) in the presence of $HOAc_F$ supports a two-step reaction mechanism, where $HOAc_F$ associates to **1** to form $[LCu^{II}(O_2^{\bullet-})(HOAc_F)]^+$ (**2**), and this complex is responsible for facilitating the electron transfer/oxidation of the substituted ferrocene. A question arises as to the identity of the electron accepting orbital and if this resides on the Cu(II) metal ion, the superoxide $O_2^{\bullet-}$ moiety, or a $[Cu-O_2]^+$ molecular orbital. Our calculations indicate that the electron accepting orbital (LUMO of **2**; see Figure S18) is the superoxide π^*_v orbital. The associated proton on the $HOAc_F$ moiety in **2** is poised for rapid proton transfer that is triggered upon one electron reduction.

It is important to mention that the hydrogen bonding interactions in $[LCu^{II}(O_2^{\bullet-})(HOAc_F)]^+$ (**2**) are proposed to be to the distal oxygen atom of the cupric superoxo moiety. The interaction with this particular O-atom may be crucial in accessing the electron transfer reactivity. In related cupric hydroperoxide complexes (i.e., the one e^-/H^+ reduced form of $[LCu^{II}(O_2^{\bullet-})]^+$) also possessing tripodal tetradentate chelates, Masuda and co-workers elegantly demonstrated that the positioning of ligand pendant hydrogen bonding amide N−H moieties in relation to the dioxygen fragment dictated the stability and physical properties of the $[(ligand)Cu^{II}(OOH)]^{2+}$ complex (Figure 15A). For H-bonding interaction with the proximal "O"-atom, a stabilizing interaction is observed, and in one case, the cupric hydroperoxide complex could be crystallographically characterized.[48] However, when H-bonding occurred to the distal "O"-atom, an increased O−O bond stretching frequency was observed and the complex had markedly lower stability, decomposing ∼3 times faster than for the case where H-bonding was absent.[49] In iron (bio)chemistry, interactions with the distal oxygen atom of ferric hydroperoxo complexes ($Fe^{III}-OOH$) can facilitate O−O bond cleavage, such as in cytochrome P450 monooxygenase[3b]

dx.doi.org/10.1021/ja4065377 | J. Am. Chem. Soc. 2013, 135, 16454−16467

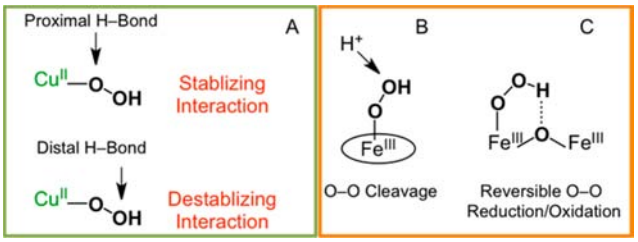

Figure 15. Interactions with the proximal vs distal O-atom in metal hydroperoxide coordination complexes. See text for further discussion and explanation.

(Figure 15B) and non-heme[50] synthetic systems undergoing conversion to Fe^{IV}=O products. A further related system is where distal O-atom proton transfer occurs during the dioxygen binding event in the non-heme diiron dioxygen-transport protein hemerythrin, Fe^{II}–OH–Fe^{II} → Fe^{III}–OOH···(O)–Fe^{III} (Figure 15C).[51]

As mentioned, the reduction/protonation of $[LCu^{II}(O_2^{\bullet-})]^+$ (**1**) to give the Cu^{II}–OOH product (Figure 2) can be effected by Me_8Fc, where the Me_8Fc/Me_8Fc^+ couple has a reduction equal to +0.120 V vs SCE (0.370 V vs NHE), but the even weaker reductant Me_2Fc ($E°$ = +0.435 vs SCE)[52] does not effect reduction of $[LCu^{II}(O_2^{\bullet-})(HOAc_F)]^+$ (**2**), allowing us to bracket the reduction potential at +0.120 < $E_{1/2}$ < +0.435 V vs SCE. The present meaning of this reaction's standard reduction potential ($E°$) is unclear (i) because of the experimental conditions employed (MeTHF solvent at low temperature) and (ii) because the process is in some manner coupled to a proton transfer event; the chemistry certainly does not comprise a pure outer-sphere electron transfer event. We can nevertheless conclude that the reaction $[LCu^{II}(O_2^{\bullet-})(HOAc_F)]^+ + e^- \rightleftharpoons [Cu^{II}–OOH]^+$ is not a highly "uphill" process and the reaction of cupric–superoxo intermediates by reductants such as the coordinated cysteine cross-linked tyrosine ArOH group (in GO) or the aminosemiquinone radical in CAO's (see Introduction) may well be expected to occur. Our work with the present cupric–superoxo complex **1** indicates that a H-bond interaction or full proton donor is also required.

An interesting corollary to these observations is that the reverse reaction, oxidation of a $[Cu^{II}–OOH]^+$ moiety, may also be possible within biological milieu. Such a situation could help explain an atmospheric dioxygen exchange pathway observed by Blackburn and co-workers in the enzyme PHM (see Figure 16).[13b] The PHM active site was shown to separately display catalase activity, implying that a peroxide to O_2 step can occur. This peroxide plus oxidized-enzyme chemistry in PHM diverges from the situation observed in heme and non-heme iron enzymes (e.g., cytochrome P450 monooxygenase, soluble methane monooxygenase, and naphthalene 1,2-dioxygenases) which undergo "peroxide shunt" biochemistry.[3b,53] There, no peroxide oxidation (to O_2) occurs, and only formation of O–O cleaved higher valent oxidizing intermediates formed from metal(s)/H_2O_2 interactions.

In summary, we have described the synthesis and characterization of a mononuclear copper/O_2 adduct possessing an acidic moiety (as the form of a neutral $HOAc_F$ molecule) which is in proximity to and directly interacting with the cupric superoxo ($Cu^{II}–O_2^{\bullet-}$) fragment. The hydrogen bonding interactions in this complex result in little structural rearrangement and no change in spin state of the complex. The copper remains in a pseudo-trigonal-bipyramidal geometry with the copper superoxo moiety in the triplet electronic ground state coordinated to the copper ion in end-on fashion. However, the H-bonding interaction to the superoxo moiety plays a vital role in altering the chemistry of the dioxygen fragment. As described above, the association of $HOAc_F$ to the superoxo moiety in **2** leads to a longer and weaker O–O bond, but a polarization effect induced by the adjacent full trifluoroacetic acid molecule causes an observed *increase* of 29 cm^{-1} in the O–O stretching frequency.

This pre-equilibrium acid association to $[LCu^{II}(O_2^{\bullet-})]^+$ (**1**) leads to novel chemical reactivity, the oxidation of outer-sphere electron transfer reduction of $[LCu^{II}(O_2^{\bullet-})(HOAc_F)]^+$ (**2**) to yield hydrogen peroxide (H_2O_2). This work begins to provide previously unavailable information and insights into the magnitude and nature of reduction potentials and relative pK_a's involved in the interconversion of molecular oxygen and peroxide as it relates to (i) biological transformations facilitated by copper oxidases/monooxygenases and (ii) practical copper ion mediated oxidative processes possibly including dioxygen fuel cell technologies. To probe for detailed and deeper insights into the PCET superoxide reduction/protonation chemistry described here, further investigations needed are kinetics (i) employing reductants with a wider range of redox potentials and (ii) with variations of the acid-proton source. Notably, the electron and proton that both end up on the copper(II)

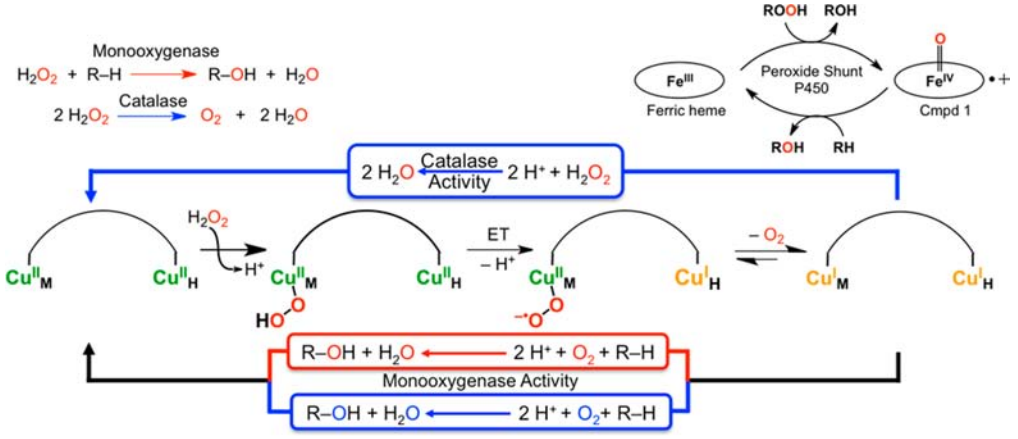

Figure 16. Proposed pathway for O_2 scrambling and incorporation of unlabeled oxygen (O_2 in blue) via substrate hydroxylation, as observed by Blackburn and co-workers,[13b] when the fully oxidized form of PHM is exposed to labeled hydrogen peroxide (H_2O_2 (in red)).

dx.doi.org/10.1021/ja4065377 | J. Am. Chem. Soc. 2013, 135, 16454–16467

coordinated $O_2^{\bullet-}$ species are derived from different sources, the former from an outer-sphere ferrocenyl reducing agent and the latter from the associated H-bonded $HOAc_F$ molecule.

■ ASSOCIATED CONTENT

Supporting Information

The full listing of authors for ref 29, reduction potentials for metallocene derivatives in MeTHF, synthetic protocol and X-ray crystal structure of the cationic portion of $[LCu^{II}Cl][B(C_6F_5)_4]$ in CIF format, supplemental figures described in the text, and the coordinates for DFT calculated metal complexes. This material is available free of charge via the Internet at http://pubs.acs.org.

■ AUTHOR INFORMATION

Corresponding Authors

edward.solomon@stanford.edu.
karlin@jhu.edu.

Notes

The authors declare no competing financial interest.

■ ACKNOWLEDGMENTS

We are grateful to the NIH (E.I.S., Grant DK31450; K.D.K., Grant GM28962; K.O.H., Grant P41RR001209; and a postdoctoral fellowship to R.E.C., Grant GM105288) for research support. Portions of this research were carried out at the Stanford Synchrotron Radiation Lightsource, a Directorate of SLAC National Accelerator Laboratory and an Office of Science User Facility operated for the U.S. Department of Energy Office of Science by Stanford University. The SSRL Structural Molecular Biology Program is supported by the DOE Office of Biological and Environmental Research and by the National Institutes of Health, National Institute of General Medical Sciences (including Grant P41GM103393), and the National Center for Research Resources (Grant P41RR001209). S.F. acknowledges the Japanese JSPS (20108010) and the JST (ALCA) for support. We also thank Ted King from TgK Scientific Limited (U.K.) for his technical support and assistance with the stopped-flow instrument and use of the 300−1100 nm extended wavelength diode array detector.

■ REFERENCES

(1) (a) Vielstch, W.; Lamm, A.; Gasteiger, H. A. *Handbook of Fuel Cells: Fundamentals, Technology and Applications*; Wiley: Hoboken, NJ, 2003. (b) Marković, N. M.; Schmidt, T. J.; Stamenković, V.; Ross, P. N. *Fuel Cells* **2001**, *1*, 105−116. (c) Cracknell, J. A.; Vincent, K. A.; Armstrong, F. A. *Chem. Rev.* **2008**, *108*, 2439−2461.

(2) (a) Gewirth, A. A.; Thorum, M. S. *Inorg. Chem.* **2010**, *49*, 3557−3566. (b) Thorseth, M. A.; Tornow, C. E.; Tse, E. C. M.; Gewirth, A. A. *Coord. Chem. Rev.* **2013**, *257*, 130−139. (c) Fukuzumi, S.; Yamada, Y.; Karlin, K. D. *Electrochim. Acta* **2012**, *82*, 493−511. (d) Solomon, E. I.; Kjaergaard, C. H.; Heppner, D. E. Molecular Properties and Reaction Mechanism in Multicopper Oxidases Related to Their Use in Biofuel Cell. In *Electrochemical Processes in Biological Systems*; John Wiley and Sons: Hoboken, NJ; in press.

(3) (a) Sono, M.; Roach, M. P.; Coulter, E. D.; Dawson, J. H. *Chem. Rev.* **1996**, *96*, 2841−2887. (b) Ortiz de Montellano, P. R. *Cytochrome P-450: Structure, Mechanism and Biochemistry*, 3rd ed.; Kluwer Academic/Plenum Publishers: New York, 2005.

(4) (a) Sheldon, R. A.; Kochi, J. K. *Metal-Catalyzed Oxidations of Organic Compounds*; Academic Press: New York, 1981. (b) *Metal Ion Activation of Dioxygen: Metal Ions in Biology*; Spiro, T. G., Ed.; Wiley-Interscience: New York, 1981; Vol. 3. (c) Sheldon, R. A. History of Oxygen Activation 1773−1993. In *The Activation of Dioxygen and Homogeneous Catalytic Oxidation*; Barton, D. H. R., Martell, A. E., Sawyer, D. T., Eds.; Plenum Press: New York, 1993; pp 9−30. (d) Lee, D.; Lippard, S. J. Nonheme Di-Iron Enzymes. In *Bio-Coordination Chemistry*; Que, L., Jr., Tolman, W. B., Eds.; Elsevier Ltd.: Oxford, U.K., 2004; Vol. *8*; pp 309−342. (e) Costas, M.; Mehn, M. P.; Jensen, M. P.; Que, L. *Chem. Rev.* **2004**, *104*, 939−986.

(5) (a) Solomon, E. I.; Sundaram, U. M.; Machonkin, T. E. *Chem. Rev.* **1996**, *96*, 2563−2605. (b) Solomon, E. I.; Ginsbach, J. W.; Heppner, D. E.; Kieber-Emmons, M. T.; Kjaergaard, C. H.; Smeets, P. J.; Tian, L.; Woertink, J. S. *Faraday Discuss.* **2011**, *148*, 11−39. (c) *Copper Proteins: Metal Ions in Biology*; Spiro, T. G., Ed.; Wiley-Interscience: New York, 1981; Vol. 3. (d) *Bioinorganic Chemistry of Copper*; Karlin, K. D., Tyeklár, Z., Eds.; Chapman & Hall: New York, 1993. (e) *Copper−Oxygen Chemistry*; Itoh, S., Karlin, K. D., Eds.; John Wiley & Sons, Inc.: Hoboken, NJ, 2011.

(6) (a) Klinman, J. P. *Chem. Rev.* **1996**, *96*, 2541−2561. (b) Klinman, J. P. *J. Biol. Chem.* **2006**, *281*, 3013−3016.

(7) Prigge, S. T.; Eipper, B.; Mains, R.; Amzel, L. M. *Science* **2004**, *304*, 864−867.

(8) (a) Babcock, G. T.; Wikström, M. *Nature* **1992**, *356*, 301−309. (b) Ferguson-Miller, S.; Babcock, G. T. *Chem. Rev.* **1996**, *96*, 2889−2908.

(9) Wilmot, C. M.; Hajdu, J.; McPherson, M. J.; Knowles, P. F.; Phillips, S. E. V. *Science* **1999**, *286*, 1724−1728.

(10) For proteins or synthetic systems involving two or more copper(I) ions, simultaneous two-electron transfer to O_2 to form a peroxo intermediate may occur. See, for example, the following: (a) Metz, M.; Solomon, E. I. *J. Am. Chem. Soc.* **2001**, *123*, 4398−4950. (b) Solomon, E. I.; Augustine, A. J.; Yoon, J. *Dalton Trans.* **2008**, 3921−3932.

(11) Humphreys, K. J.; Mirica, L. M.; Wang, Y.; Klinman, J. P. *J. Am. Chem. Soc.* **2009**, *131*, 4657−4663.

(12) Liu, Y.; Mukherjee, A.; Nahumi, N.; Ozbil, M.; Brown, D.; Angeles-Boza, A. M.; Dooley, D. M.; Prabhakar, R.; Roth, J. P. *J. Phys. Chem. B* **2012**, *117*, 218−229.

(13) (a) Chen, P.; Solomon, E. I. *J. Am. Chem. Soc.* **2004**, *126*, 4991−5000. (b) Bauman, A. T.; Yukl, E. T.; Alkevich, K.; McCormack, A. L.; Blackburn, N. J. *J. Biol. Chem.* **2006**, *281*, 4190−4198. (c) Chen, P.; Solomon, E. I. *Proc. Nat. Acad. Sci. U.S.A.* **2004**, *101*, 13105−13110.

(14) (a) Crespo, A.; Marti, M. A.; Roitberg, A. E.; Amzel, L. M.; Estrin, D. A. *J. Am. Chem. Soc.* **2006**, *128*, 12817−12828. (b) Yoshizawa, K.; Kihara, N.; Kamachi, T.; Shiota, Y. *Inorg. Chem.* **2006**, *45*, 3034−3041. (c) McIntyre, N. R.; Lowe, E. W.; Merkler, D. J. *J. Am. Chem. Soc.* **2009**, *131*, 10308−10319.

(15) (a) Quinlan, R. J.; Sweeney, M. D.; Lo Leggio, L.; Otten, H.; Poulsen, J.-C. N.; Johansen, K. S.; Krogh, K. B. R. M.; Jørgensen, C. I.; Tovborg, M.; Anthonsen, A.; Tryfona, T.; Walter, C. P.; Dupree, P.; Xu, F.; Davies, G. J.; Walton, P. H. *Proc. Nat. Acad. Sci. U.S.A.* **2011**, *108*, 15079−15084. (b) Phillips, C. M.; Beeson, W. T.; Cate, J. H.; Marletta, M. A. *ACS Chem. Biol.* **2011**, *6*, 1399−1406. (c) Beeson, W. T.; Phillips, C. M.; Cate, J. H. D.; Marletta, M. A. *J. Am. Chem. Soc.* **2012**, *134*, 890−892. (d) Li, X.; Beeson, W. T., IV; Phillips, C. M.; Marletta, M. A.; Cate, J. H. D. *Structure* **2012**, *20*, 1051−1061. (e) Hemsworth, G. R.; Taylor, E. J.; Kim, R. Q.; Gregory, R. C.; Lewis, S. J.; Turkenburg, J. P.; Parkin, A.; Davies, G. J.; Walton, P. H. *J. Am. Chem. Soc.* **2013**, *135*, 6069−6077.

(16) (a) Lewis, E. A.; Tolman, W. B. *Chem. Rev.* **2004**, *104*, 1047−1076. (b) Mirica, L. M.; Ottenwaelder, X.; Stack, T. D. P. *Chem. Rev.* **2004**, *104*, 1013−1045. (c) Quant Hatcher, L.; Karlin, K. D. *J. Biol. Inorg. Chem.* **2004**, *9*, 669−683. (d) Itoh, S. *Curr. Opin. Chem. Biol.* **2006**, *10*, 115−122.

(17) (a) Fujisawa, K.; Tanaka, M.; Morooka, Y.; Kitajima, N. *J. Am. Chem. Soc.* **1994**, *116*, 12079−12080. (b) Chen, P.; Root, D. E.; Campochiaro, C.; Fujisawa, K.; Solomon, E. I. *J. Am. Chem. Soc.* **2003**, *125*, 466−474.

(18) (a) Jazdzewski, B. A.; Reynolds, A. M.; Holland, P. L.; Young, V. G.; Kaderli, S.; Zuberbuehler, A. D.; Tolman, W. B. *JBIC, J. Biol. Inorg. Chem.* **2003**, *8*, 381−393. (b) Donoghue, P. J.; Gupta, A. K.; Boyce, D.

W.; Cramer, C. J.; Tolman, W. B. *J. Am. Chem. Soc.* **2010**, *132*, 15869−15871.
(19) (a) Schatz, M.; Raab, V.; Foxon, S. P.; Brehm, G.; Schneider, S.; Reiher, M.; Holthausen, M. C.; Sundermeyer, J.; Schindler, S. *Angew. Chem., Int. Ed.* **2004**, *43*, 4360−4363. (b) Würtele, C.; Gaoutchenova, E.; Harms, K.; Holthausen, M. C.; Sundermeyer, J.; Schindler, S. *Angew. Chem., Int. Ed.* **2006**, *45*, 3867−3869. (c) Lanci, M. P.; Smirnov, V. V.; Cramer, C. J.; Gauchenova, E. V.; Sundermeyer, J.; Roth, J. P. *J. Am. Chem. Soc.* **2007**, *129*, 14697−14709.
(20) (a) Kunishita, A.; Kubo, M.; Sugimoto, H.; Ogura, T.; Sato, K.; Takui, T.; Itoh, S. *J. Am. Chem. Soc.* **2009**, *131*, 2788−2789. (b) Kunishita, A.; Ertem, M. Z.; Okubo, Y.; Tano, T.; Sugimoto, H.; Ohkubo, K.; Fujieda, N.; Fukuzumi, S.; Cramer, C. J.; Itoh, S. *Inorg. Chem.* **2012**, *51*, 9465−9480. (c) Kobayashi, Y.; Ohkubo, K.; Nomura, T.; Kubo, M.; Fujieda, N.; Sugimoto, H.; Fukuzumi, S.; Goto, K.; Ogura, T.; Itoh, S. *Eur. J. Inorg. Chem.* **2012**, *2012*, 4574−4578.
(21) (a) Maiti, D.; Fry, H. C.; Woertink, J. S.; Vance, M. A.; Solomon, E. I.; Karlin, K. D. *J. Am. Chem. Soc.* **2007**, *129*, 264−265. (b) Maiti, D.; Lee, D.-H.; Gaoutchenova, K.; Würtele, C.; Holthausen, M. C.; Sarjeant, A. A. N.; Sundermeyer, J.; Schindler, S.; Karlin, K. D. *Angew. Chem., Int. Ed.* **2008**, *47*, 82−85. (c) Woertink, J. S.; Tian, L.; Maiti, D.; Lucas, H. R.; Himes, R. A.; Karlin, K. D.; Neese, F.; Würtele, C.; Holthausen, M. C.; Bill, E.; Sundermeyer, J.; Schindler, S.; Solomon, E. I. *Inorg. Chem.* **2010**, *49*, 9450−9459. (d) Peterson, R. L.; Himes, R. A.; Kotani, H.; Suenobu, T.; Tian, L.; Siegler, M. A.; Solomon, E. I.; Fukuzumi, S.; Karlin, K. D. *J. Am. Chem. Soc.* **2011**, *133*, 1702−1705.
(22) Kunishita, A.; Ishimaru, H.; Nakashima, S.; Ogura, T.; Itoh, S. *J. Am. Chem. Soc.* **2008**, *130*, 4244−4245.
(23) Dines, M. B. *Inorg. Chem.* **1972**, *11*, 2949−2952.
(24) LeSuer, R. J.; Buttolph, C.; Geiger, W. E. *Anal. Chem.* **2004**, *76*, 6395−6401.
(25) Li, C.-D.; Mella, S. L.; Sartorelli, A. C. *J. Med. Chem.* **1981**, *24*, 1089−1092.
(26) Tenderholt, A.; Hedman, B.; Hodgson, K. O. *PySpline*; Stanford Synchrotron Radiation Laboratory: Stanford, CA, 2006.
(27) George, G. N. *EXAFSPAK*; Stanford Synchrotron Radiation Laboratory: Stanford, CA, 2000.
(28) Rehr, J. J.; Albers, R. C. *Rev Mod Phys* **2000**, *72*, 621−654.
(29) Frisch, M. J.; et al.. *Gaussian 09*, revision C.01; Gaussian, Inc.: Wallingford, CT, 2009. For the full reference, see the Supporting Information.
(30) (a) Becke, A. D. *J. Chem. Phys.* **1993**, *98*, 5648−5652. (b) Lee, C. T.; Yang, W. T.; Parr, R. G. *Phys. Rev. B* **1988**, *37*, 785−789. (c) Stephens, P. J.; Devlin, F. J.; Chabalowski, C. F.; Frisch, M. J. *J. Phys. Chem.* **1994**, *98*, 11623−11627.
(31) *NIST Computational Chemistry Comparison and Benchmark Database*; Johnson, R. D., Ed.; NIST Standard Reference Database Number 101 Release 15b; National Institute of Standards and Technology: Gaithersburg, MD, August 2011; http://cccbdb.nist.gov/.
(32) Gorelsky, S. I. *SWizard*, version 4.2; University of Ottawa: Ottawa, Ontario, Canada, 2013; http://www.sg-chem.net/swizard/.
(33) Kieber-Emmons, M. T. *Lumo*, version 1.0.1; Ephrata, PA, 2012; http://www.kieber-emmons.com/Lumo/.
(34) Tenderholt, A. L. *QMForge*, version 2.1; Stanford University: Stanford, CA, USA.
(35) Itoh, S. Chemical Reactivity of Copper Active-Oxygen Complexes. In *Copper−Oxygen Chemistry*; Itoh, S., Karlin, K. D., Eds.; John Wiley & Sons, Inc.: Hoboken, NJ, 2011; pp 225−282.
(36) Liang, H.-C.; Karlin, K. D.; Dyson, R.; Kaderli, S.; Jung, B.; Zuberbühler, A. D. *Inorg. Chem.* **2000**, *39*, 5884−5894.
(37) (a) Spencer, D. J. E.; Aboelella, N. W.; Reynolds, A. M.; Holland, P. L.; Tolman, W. B. *J. Am. Chem. Soc.* **2002**, *124*, 2108−2109. (b) Reynolds, A. M.; Gherman, B. F.; Cramer, C. J.; Tolman, W. B. *Inorg. Chem.* **2005**, *44*, 6989−6997. (c) Aboelella, N. W.; Kryatov, S. V.; Gherman, B. F.; Brennessel, W. W.; Young, V. G.; Sarangi, R.; Rybak-Akimova, E. V.; Hodgson, K. O.; Hedman, B.; Solomon, E. I.; Cramer, C. J.; Tolman, W. B. *J. Am. Chem. Soc.* **2004**, *126*, 16896−16911.
(38) (a) Lee, Y.-M.; Kotani, H.; Suenobu, T.; Nam, W.; Fukuzumi, S. *J. Am. Chem. Soc.* **2008**, *130*, 434−435. (b) Connelly, N. G.; Geiger, W. E. *Chem. Rev.* **1996**, *96*, 877−910.
(39) See Supporting Information.
(40) Smith, D. W.; Andrews, L. *J. Chem. Phys.* **1974**, *60*, 81−85.
(41) Fry, H. C.; Scaltrito, D. V.; Karlin, K. D.; Meyer, G. J. *J. Am. Chem. Soc.* **2003**, *125*, 11866−11871.
(42) Overlap in the diamagnetic region for that of pure $^{2}HOAc_{F}$ (in a separate experiment) and **2** is observed.
(43) Thermal decomposition of this reaction mixture leads to a loss of both the fluorine resonances attributed to free $HOAc_{F}$ and $[LCu^{II}(O_2^{\bullet-})(HOAc_{F})]^{+}$ with a less intense asymmetric signal centered at −76.5 ppm (see Supporting Information).
(44) DuBois, J. L.; Mukherjee, P.; Collier, A. M.; Mayer, J. M.; Solomon, E. I.; Hedman, B.; Stack, T. D. P.; Hodgson, K. O. *J. Am. Chem. Soc.* **1997**, *119*, 8578−8579.
(45) (a) Kitajima, N.; Fujisawa, K.; Fujimoto, C.; Moro-oka, Y.; Hashimoto, S.; Kitagawa, T.; Toriumi, K.; Tasumi, K.; Nakamura, A. *J. Am. Chem. Soc.* **1992**, *114*, 1277−1291. (b) Mahapatra, S.; Halfen, J. A.; Wilkinson, E. C.; Pan, G.; Wang, X.; Young, V. G., Jr.; Cramer, C. J.; Que, J., L.; Tolman, W. B. *J. Am. Chem. Soc.* **1996**, *118*, 11555−11574.
(46) We also considered a variation of model 2D where the proton is transferred to the superoxo (i.e., $Cu^{II}OOH\cdots OAc_{F}$ instead of $Cu^{II}OO\cdots HOAc_{F}$); however, this species was not stable and converted to 2D upon geometry optimization (Figure S19).
(47) For this calculation, we used the Mulliken charges calculated from full model 2D as the magnitude of the point charges placed at $HOAc_{F}$ atomic coordinates.
(48) Wada, A.; Harata, M.; Hasegawa, K.; Jitsukawa, K.; Masuda, H.; Mukai, M.; Kitagawa, T.; Einaga, H. *Angew. Chem., Int. Ed.* **1998**, *37*, 798−799.
(49) Yamaguchi, S.; Nagatomo, S.; Kitagawa, T.; Funahashi, Y.; Ozawa, T.; Jitsukawa, K.; Masuda, H. *Inorg. Chem.* **2003**, *42*, 6968−6970.
(50) (a) Li, F.; England, J.; Que, L., Jr. *J. Am. Chem. Soc.* **2010**, *132*, 2134−2135. (b) Kovacs and co-workers recently reported the proton dependent oxidative addition of superoxide (as hydroperoxyl radical ($^{\bullet}$OOH)) to a mononuclear non-heme Fe^{II} thiolate complex resulting in the formation of a stable ferric−hydroperoxo (Fe^{III}−OOH) complex at −78 °C. Hydrogen peroxide could be liberated from this species by the addition of acetic acid or other strong acids. See the following: Nam, E.; Alokolaro, P. E.; Swartz, R. D.; Gleaves, M. C.; Pikul, J.; Kovacs, J. A. *Inorg. Chem.* **2011**, *50*, 1592−1602.
(51) Brunold, T. C.; Solomon, E. I. *J. Am. Chem. Soc.* **1999**, *121*, 8288−8295.
(52) Pavlishchuk, V. V.; Addison, A. W. *Inorg. Chim. Acta* **2000**, *298*, 97−102.
(53) (a) Wallar, B. J.; Lipscomb, J. D. *Chem. Rev.* **1996**, *96*, 2625−2658. (b) Wade, R. S.; Castro, C. E. *Chem. Res. Toxicol.* **1996**, *9*, 1382−1390.